JACS Au
AN OPEN ACCESS JOURNAL OF THE AMERICAN CHEMICAL SOCIETY

pubs.acs.org/jacsau
Article

A Spectroscopic Criterion for Identifying the Degree of Ground-Level Near-Degeneracy Derived from Effective Hamiltonian Analyses of Three-Coordinate Iron Complexes

Wang Chen,[○] Nikolai Kochetov,[○] Thomas Lohmiller, Qing Liu, Liang Deng,* Alexander Schnegg,* and Shengfa Ye*

Cite This: JACS Au 2025, 5, 1016−1030
Read Online

ACCESS | Metrics & More | Article Recommendations | Supporting Information

ABSTRACT: The fascinating magnetic and catalytic properties of coordinatively unsaturated 3d metal complexes are a manifestation of their electronic structures, in particular their nearly doubly or triply degenerate orbital ground levels. Here, we propose a criterion to determine the degree of degeneracy of this class of complexes based on their experimentally accessible magnetic anisotropy (parametrized by the electron spin *g*- and zero-field splitting (ZFS)-tensors). The criterion is derived from a comprehensive spectroscopic and theoretical study in the trigonal planar iron(0) complex, [(IMes)Fe(dvtms)] (IMes = 1,3-di(2′,4′,6′-trimethylphenyl)imidazol-2-ylidene, dvtms = divinyltetramethyldisiloxane, **1**). Accurate ZFS-values (D = +33.54 cm^{-1}, E/D = 0.09) and *g*-values ($g_{\|}$ = 1.96, $g_{\perp}$ = 2.45) of the triplet (S = 1) ground level of complex **1** were determined by complementary THz-EPR spectroscopy and SQUID magnetometry. In-depth effective Hamiltonian (EH) analyses coupled to wave-function-based *ab initio* calculations show that **1** features a ground level with three energetically close-lying orbital states with a "two-above-one" energy pattern. The observed magnetic anisotropy results from mixing of the two excited electronic states with the ground state by spin−orbit coupling (SOC). EH investigations on **1** and related complexes allowed us to generalize this finding and establish the anisotropy of the *g*- and ZFS-tensors as spectroscopic markers for assigning two- or three-fold orbital near-degeneracy.

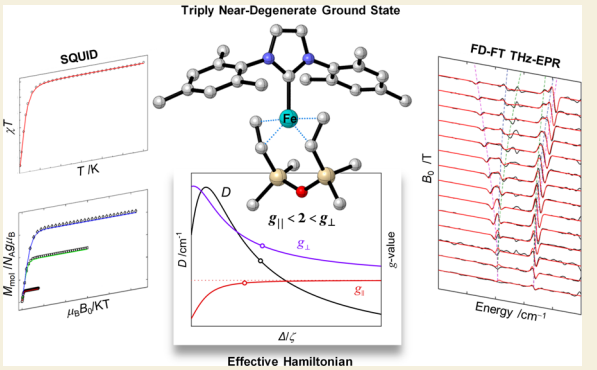

KEYWORDS: *low-coordinate complexes, orbitally near-degenerate ground level, magnetometry, THz-EPR spectroscopy, zero-field splitting, g-tensor, magneto-structural correlation, spin−orbit coupling*

INTRODUCTION

Transition-metal complexes with unsaturated coordination are intensively studied for their role as catalytic active sites and pivotal reaction intermediates in demanding chemical transformations. Isolated low-coordinate metal atoms dispersed on supports as single-atom catalysts have been reported widely to achieve high activity and selectivity.[1] In biology, N_2 binding and subsequent functionalization has been proposed to take place at the three-coordinate iron centers of the iron−molybdenum cofactor of nitrogenase.[2] In synthetic chemistry, reduction of three-coordinate iron(II) chloride complex [LFe^{II}Cl] (**2** in Chart 1, L = HC[C(^{t}Bu)N(2,6-$iPr_2C_6H_3$)]$^{2-}$) gives dinitrogen complex K_2[LFeNNFeL] and ultimately results in N−N bond cleavage.[3] Interest in three-coordinate iron(0) complexes was sparked by their successful application as catalysts for C−C bond formation reactions. These include the catalytic cross-electrophile coupling of aryl chlorides with unactivated alkyl chlorides,[4] stereoselective C−H alkylation reaction of indole derivatives,[5] and the Suzuki biaryl coupling of aryl chloride substrates with activated aryl boronic esters.[6] Furthermore, it has been shown that square-planar [Fe^{II}(TPP)] (**3**, TPP^{2-} = tetraphenylporphyrinate dianion) and its derivatives exhibit one of the highest homogeneous catalytic performances for electrochemical CO_2 reduction.[7] Combined spectroscopic and computational investigations have shown that three close lying orbital states contribute to the ground level of **3**.[8,9] Further detailed analysis of the structure−function relationship identified this extraordinary electronic structure as a key factor for the extensive CO_2 reduction activity of complex **3**.[10] Hereafter, for clarity we differentiate the terms level and state, in that an energy level of

Received: December 22, 2024
Revised: January 24, 2025
Accepted: January 27, 2025
Published: February 6, 2025

Chart 1. Low-Coordinate Complexes under Investigation

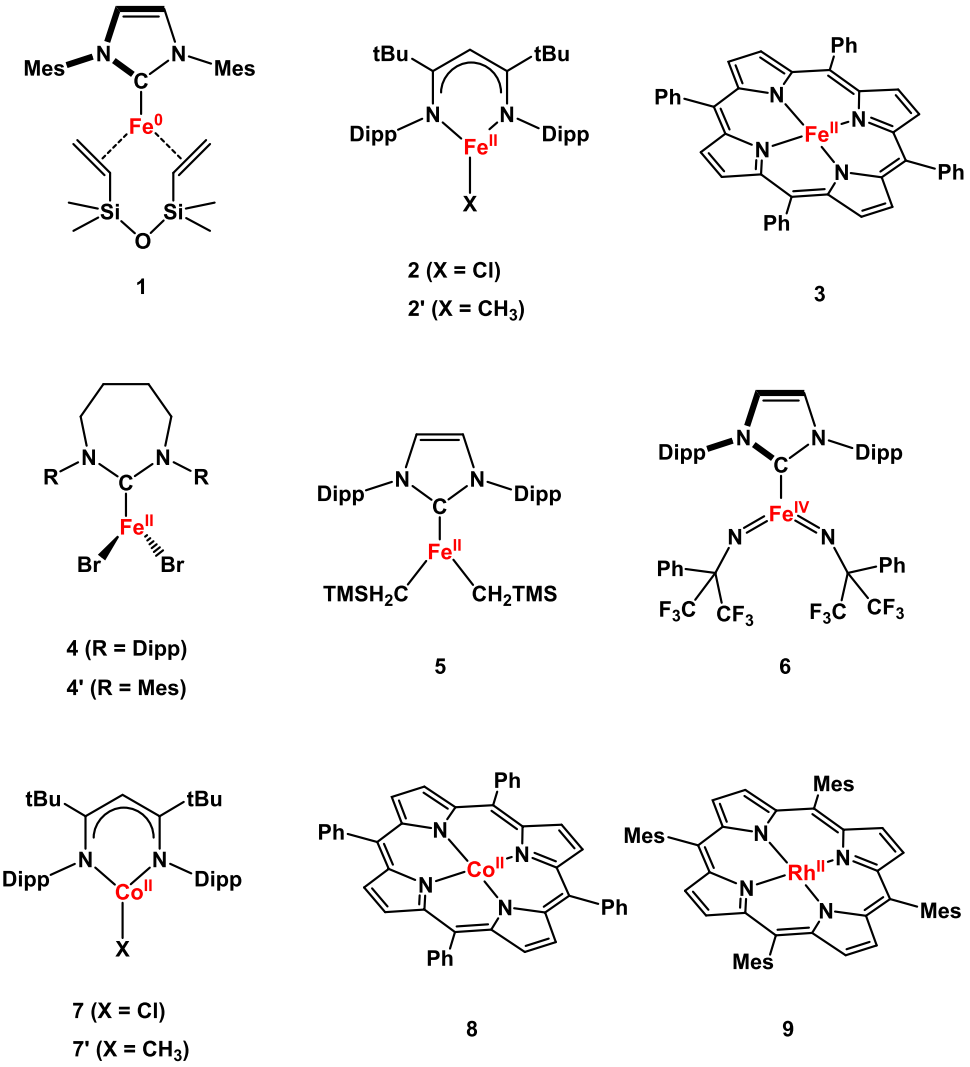

a system with orbital degeneracy may possess several different constituent orbital states.

Energetically almost degenerate d orbitals are a consequence of the very weak ligand fields in coordinatively unsaturated 3d complexes. The resulting electronic structures not only determine their chemical properties, but also their often very large magnetic anisotropies. The latter property renders them potential building blocks for the synthesis of molecular nanomagnets.[11] As typical examples, a series of two-coordinate high-spin Fe(I/II)[12] and Co(I/II)[13] complexes were identified as single-molecule magnets with very large magnetic anisotropies, which has been traced back to the presence of two-fold near-degeneracy in the ground level.

Three-coordinate complexes can also exhibit pronounced magnetic anisotropies, but correlation with their structures is less obvious at first sight. For instance, trigonal planar high-spin iron(II) complexes [Fe(7-Dipp)Br_2] (7-Dipp = 1,3-bis(2,6-diisopropylphenyl)-4,5,6,7-tetrahydro-[1,3]-diazepin-2-ylidene, **4**), [Fe(7-Mes)Br_2] (7-Mes = 1,3-bis(2,4,6-trimethylphenyl)-4,5,6,7-tetrahydro-[1,3]-diazepin-2-ylidene, **4′**) and [(IPr)Fe(CH_2TMS)$_2$] (IPr = 1,3-bis(2′,6′-diisopropylphenyl)-imidazol-2-ylidene, CH_2TMS = bis(trimethylsilyl)methyl, **5**) (Chart 1), all stabilized by a cyclic NHC ligand, share similar geometric structures but exhibit disparate magnetic properties. Easy-plane magnetic anisotropy is found for **4** and **4′**, while **5** features easy-axis magnetic anisotropy.[14] As elaborated below, the differing magnetic anisotropies measured for complexes **4**, **4′** and **5** result from the distinct orbital near-degeneracy of their ground levels.

Undoubtedly, both chemical activities and magnetic properties of coordinatively unsaturated metal complexes are determined by their peculiar electronic structures, more precisely, critically hinged on the degree of orbital degeneracy of their ground levels. In principle, exact orbital degeneracy cannot exist, because inevitable Jahn−Teller or Renner−Teller distortions will lift the orbital degeneracy and hence the resulting state degeneracy to a certain extent.[15] Concurrently, spin−orbit coupling (SOC) within this manifold of pseudo-degenerate orbital states, if present, tends to restore the orbital degeneracy and gives rise to first-order orbital angular momentum in the ground level.

In earlier work,[16] orbitally near-degenerate systems were proposed to be distinguished by $\Delta E < 10\zeta$, where ΔE is the nonrelativistic energy separation between the ground and the lowest-energy d-d excited state, and ζ the effective one-electron SOC constant of the metal center. It follows from this criterion that, even under a zeroth-order approximation, the SOC among different components of orbital states in the ground

https://doi.org/10.1021/jacsau.4c01256
JACS Au 2025, 5, 1016−1030

level has to be treated on an equal footing with the ligand field splitting, since both interactions are of the same order of magnitude. In contrast, for orbitally nondegenerate complexes, the SOC between the ground and excited levels can be adequately approximated as a perturbation, as well-documented in the literature.[17]

Strictly speaking, ΔE is not an experimental observable, because the associated ligand-field electronic transition measured experimentally includes SOC effects. Even so, such a transition is, however, intrinsically electric dipole forbidden. Thus, its low intensity renders the detection difficult in the near-infrared region ($\Delta E < 10^4$ cm^{-1}), considering the magnitude of ζ for 3d transition metals. Furthermore, the relation between ΔE and ζ is not sufficient to determine the degree of ground-level degeneracy, i.e. the presence of two or more energetically close lying states. Therefore, a more practical criterion is required that identifies not only the existence of ground-level orbital near-degeneracy but also the degree of it.

Herein, we close this gap by a new criterion to identify the presence and degree of ground-level degeneracy from experimentally determined metal-ion magnetic-anisotropy (*g*- and ZFS-tensors). The starting point of our study was the establishment of a detailed magneto-structural correlation in the three-coordinate Fe complex [(IMes)Fe(dvtms)] (IMes = 1,3-di(2′,4′,6′-trimethylphenyl)imidazol-2-ylidene, dvtms = divinyltetramethyldisiloxane, **1**), stabilized by a ligand set of an NHC and two alkenes.[18] Accurate magnetic characterization of complex **1** was obtained, by measuring the *g*- and ZFS-values by complementary SQUID magnetometry and broadband Frequency-Domain Fourier-Transform THz-EPR (FD-FT THz-EPR). Quantum chemical calculations established a correlation between the measured spin Hamiltonian (SH) parameters and the electronic structure of **1**. This approach, however, does not allow the individual magneto-structural correlation derived for **1** to be readily transferred to systems with analogous electronic structures. To obtain the desired general criterion, we therefore extended our theoretical approach and introduced an effective Hamiltonian (EH)[8] coupled with wave-function-based *ab initio* calculations. This EH treats the energy differences between the orbital ground state and the low-lying excited states on the same footing as the SOC and the magnetic interactions between them. Our approach allows generalized statements to be made about the relationship between *g*- and ZFS-values and the degree of near-degeneracy of the orbital ground level. In the following, we distinguish between double and triple near-degeneracy. Triple degeneracy is further subdivided into type I, in which the energy gap between the first and the second excited state is small compared to their energy separation from the ground state, and type II, in which the distance from the ground state to the first excited state is comparable to the distance between the two excited states.

For more than half-filled shells we found that doubly degenerate levels exhibit $g_\perp < 2 < g_\parallel$ and $D < 0$, type I triply degenerate levels have $g_\parallel < 2 < g_\perp$ and $D > 0$, while type II triply degenerate levels have $g_x < 2 < g_y < g_z$ and $D < 0$. Systems having less than half-filled degenerate shells are differentiated by $g_\perp < g_\parallel < 2$ and $D > 0$ for type I triple degeneracy, $g_z < g_y < g_x < 2$ and $D < 0$ for type II triple degeneracy, and $g_\parallel < g_\perp < 2$ and $D < 0$ for double degeneracy.

In the last part of this work, we apply the newly derived criteria to related metal complexes (see Chart 1) and discuss their magneto-structural correlations.

EXPERIMENTAL SECTION

Synthesis

The complex [(IMes)Fe(dvtms)] (**1**) was synthesized according to the reported procedures.[18] For all experimental work and storage, inert gas conditions or cryogenic temperatures were maintained.

Magnetometry

Magnetic susceptibility was obtained with a superconducting quantum interference device (SQUID, MPMS-7, Quantum Design; calibrated with a standard palladium reference sample; error <2%) on powder samples of **1** immobilized in *n*-octadecane at an applied field of 1 T. Diamagnetic background arising from *n*-octadecane was subtracted from raw data. Susceptibility data is plotted as χT vs T curves. Variable-field variable-temperature (VFVT) magnetization measurements were carried out at 1, 4, and 7 T on the same SQUID magnetometer with the magnetization equidistantly sampled on a $1/T$ temperature scale in the temperature range 2−300 K.

THz-EPR Spectroscopy

FD-FT THz-EPR was performed at the THz-EPR beamline of the synchrotron user facility BESSY II.[19] The spectrometer allows for THz-EPR measurements from 0.1 to 175 THz (∼3−5800 cm^{-1}), employing a fully evacuated quasi-optical THz beamline, a high-resolution Fourier-transform infrared (FTIR) spectrometer (Bruker IFS 125HR), a superconducting high-field magnet (Oxford Spectromag 4000; B_0 = +11 to −11 T) with variable temperature insert (VTI, T = 2−300 K) and a liquid-He-cooled (4.2 K) bolometer detector (IR labs). A detailed description of the spectrometer can be found elsewhere.[20] Experimental procedures are described in the Supporting Information (SI). FD-FT THz-EPR spectra are shown as magnetic field division spectra (MDS) (Figure S1). FD-FT THz-EPR spectra are shown as magnetic field division spectra (MDS), where a spectrum obtained at an external magnetic field B_0 + 0.5 T is divided by a reference spectrum measured at B_0.

Calculational Setup

All calculations were performed with the ORCA 5.0 quantum chemical program.[21] The crystal structure of complex **1** was used in highly correlated wave-function-based *ab initio* calculations. In order to reduce the computational costs, methyl functionalities on the phenyls were substituted by hydrogens, and their positions were optimized by using the TPSSh functional[22] in combination with the def2-SVP basis set[23] for all atoms. Noncovalent interactions were accounted for using the D3BJ corrections by Grimme.[24] For complete active space self-consistent field (CASSCF)[25] computations, the active space is composed of 8 electrons distributed into orbitals including the five 3d orbitals of the Fe center and the two bonding counterparts of the Fe $d_{x^2-y^2}$ and d_{xy} molecular orbitals to account for the strong covalent interaction between the dvtms ligand and the Fe atom. In addition, the second d shell is also included into the active space to account for the double-shell effect.[26] Quasi-restricted orbitals from DFT calculations were chosen as the initial guess of the active orbitals. On top of the CASSCF wave functions, second-order N-electron valence perturbation theory (NEVPT2)[27] was employed to capture dynamic correlations. CASSCF/NEVPT2 computations used the def2-SVP basis set for C and H atoms and the def2-TZVP basis set for other atoms along with the def2/JK auxiliary basis set[28] for the RIJK approximation.[29]

RESULTS AND DISCUSSION

Determination of the Magnetic Anisotropy in 1

For precise determination of the magnetic anisotropy of **1**, χT and VFVT measurements were complemented with FD-FT THz-EPR spectroscopy (Figure 1a−c, respectively). The χT

https://doi.org/10.1021/jacsau.4c01256
JACS Au 2025, 5, 1016−1030

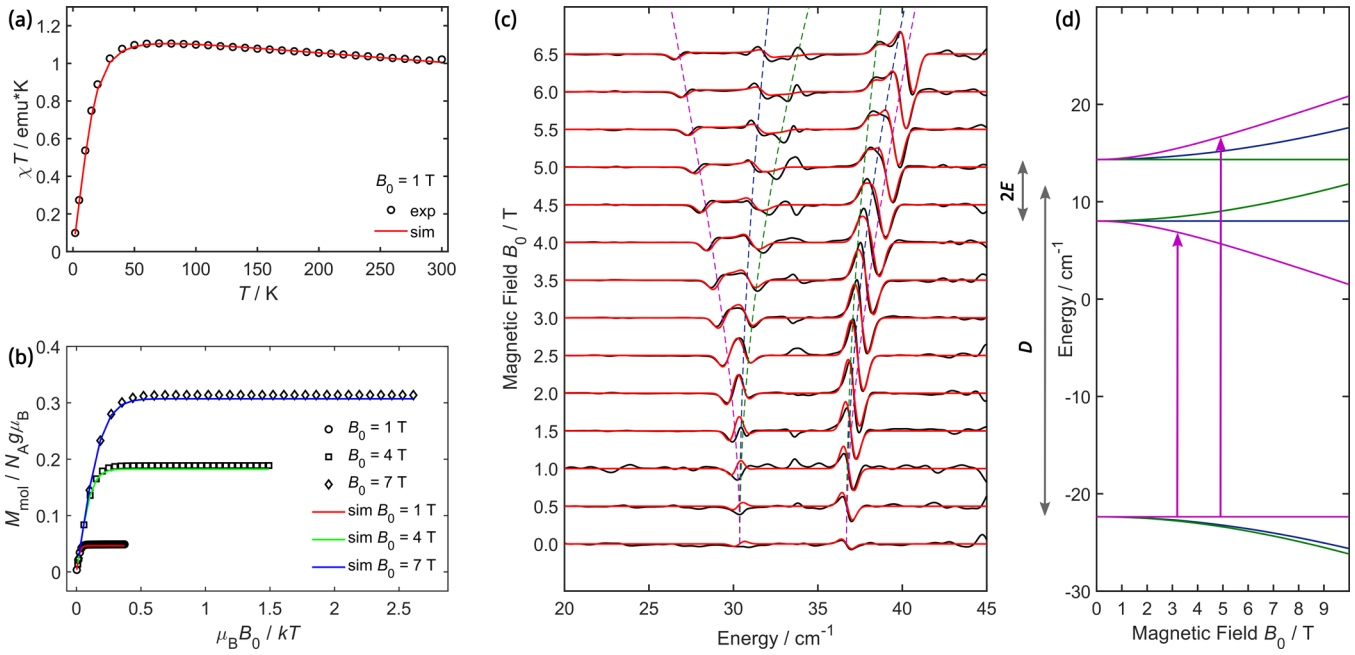

Figure 1. Magnetic characterization of **1**, (a) χT vs T at 1 T, (b) VFVT curves obtained at 1, 4 and 7 T and (c) FD-FT THz-EPR MDS at T = 4.8 K. Simulations (colored lines) obtained with eq 1 and parameters given in the text and Table S1 are plotted alongside experimental data (circles for χT, circles, squares and diamonds for VFVT data and solid black lines for FD-FT THz-EPR spectra). Dashed lines in (c) indicate simulated field dependent transition energies for $\boldsymbol{B_0}$ aligned along the x- (blue), y- (green) and z-axes (magenta) of the ZFS-tensor. (d) S = 1 spin-energy levels vs external magnetic field calculated with the same SH model and plotted with the same color code as in (c). Vertical arrows indicate allowed EPR-transitions for the z-axis projection.

curve of **1** depicted in Figure 1a exhibits a room temperature value close to 1 emu·K (μ_{eff} = 2.83 μ_B), the anticipated spin-only value for an S = 1 state. Further lowering the temperature below ∼50 K leads to a sharp drop in χT, indicating substantial ZFS. The corresponding VFVT traces at 1, 4, and 7 T are shown in Figure 1b.

For an independent and direct determination of D and E, FD-FT THz-EPR spectra of **1** were recorded at 4.8 K and at magnetic fields between B_0 = 0 and 7 T in 0.5 T steps. At low magnetic fields, two resonances are observed at 30 and 36 cm^{-1} in the MDS (Figure 1c), which shift and further split upon increasing the magnetic field. The observed resonances are assigned to $\Delta M_S = \pm 1$ transitions between the levels of the S = 1 system. As can be seen from the energy levels in Figure 1d, the center of the two transitions around ∼33 cm^{-1} corresponds to D, the axial ZFS parameter, while their separation of ∼6 cm^{-1} is determined by 2E, the rhombic part of the ZFS. The ability to unambiguously resolve D and E in the EPR spectrum allows for higher accuracy in the determination of the other SH parameters. In particular, for SQUID magnetometry, the rhombicity of the ZFS tensor is usually strongly correlated with the anisotropy of the $\boldsymbol{g}$-tensor.

Simulations were performed with the following SH model

$$\hat{\boldsymbol{H}} = D\left[\hat{S}_z^2 - \frac{1}{3}S(S+1) + \frac{E}{D}(\hat{S}_x^2 - \hat{S}_y^2)\right] + \mu_B \boldsymbol{B}_0 \boldsymbol{g} \hat{\boldsymbol{S}} \quad (1)$$

Here, the first term describes the axial and rhombic second-order ZFS interactions with parameters D and E, respectively. The coordinate system is molecule-fixed and chosen such that $0 \le E/D \le 1/3$, with the z-axis defining the dominant anisotropy direction. The second term denotes the electron-spin Zeeman interaction involving the $\boldsymbol{g}$-tensor with the main values, g_x, g_y and g_z. In the simulations, g_z is assumed as collinear to D_Z. THz-EPR spectra and magnetometry data calculated with eq 1 were fitted to the experimental traces by fit routines using the Matlab toolbox EasySpin.[30] Simulations with the best set of SH parameters are plotted in Figure 1 alongside experimental magnetometry and THz-EPR data. For the THz-EPR data, D = +33.54 cm^{-1}, E = 3.16 cm^{-1} (E/D = 0.09), $g_z = g_\parallel$ = 1.96 and $g_x = g_y = g_\perp$ = 2.45 were obtained. Note that $g_\parallel$, which defines the outer edges of the THz-EPR spectrum, can be determined with higher accuracy than $g_\perp$. Deviations of the experimental FD-FT THz-EPR spectra from the simulations around 33 cm^{-1} are assigned to spin-phonon couplings,[31] which are not considered in eq 1.

Since D and E can be directly read off from the THz-EPR spectra, these parameters were fixed while fitting the SQUID data. For the latter, best agreement between experiment and simulation was obtained for D = +33.54 cm^{-1}, E = 3.16 cm^{-1}, $g_\parallel$ = 1.97, $g_\perp$ = 2.23. Overall, excellent agreement between experiment and simulation was achieved. The slight discrepancy between the g-values obtained from best fits to the SQUID and THz-EPR data may originate from contributions of the diamagnetic matrix in which complex **1** was fixed during the SQUID experiments. Simultaneous fits of the THz-EPR and SQUID data as described by Lohmiller et al.[32] yielded nearly the same SH parameters (see Figures S2 and S3 and SH parameters in Table S1). Furthermore, simulations performed using a rhombic $\boldsymbol{g}$-tensor ($g_x \neq g_y \neq g_z$) gave as good results as with an axial $\boldsymbol{g}$-tensor only when both g_x and g_y were in the range of 2.3 to 2.5. Thus, the following relation of the g-values could be unambiguously determined $g_\parallel = g_z < 2 < g_x, g_y$ or $g_\perp$. Recently, Neidig and co-workers reported nearly identical D- and E-values for closely related three-coordinate Fe(0) bis-ethylene complexes, determined with magnetic circular dichroism spectroscopy.[33] These measurements provide

https://doi.org/10.1021/jacsau.4c01256
JACS Au 2025, 5, 1016−1030

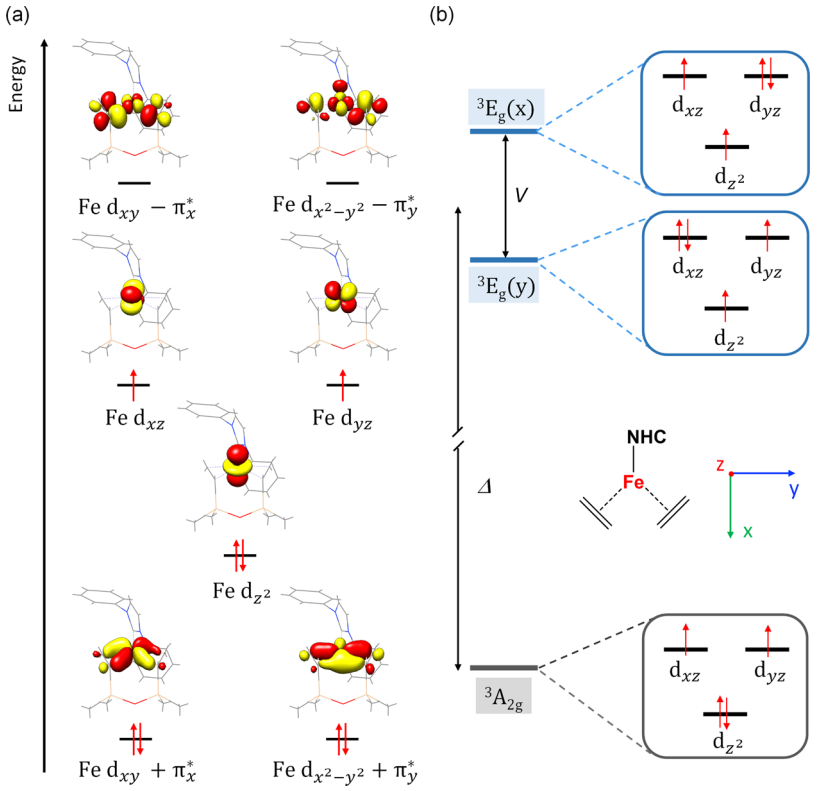

Figure 2. (a) Active orbitals and orbital occupation of the $^3A_{2g}$ ground state of **1** obtained by CASSCF calculations. (b) Low-energy spectrum with the near-degenerate orbital set of d_{z^2}, d_{xz} and d_{yz}, the resulting ground state $^3A_{2g}$ and the two excited states $^3E_g(x)$ and $^3E_g(y)$ labeled by the irreducible representations of the effective D_3 point group. Δ denotes the energy difference between the ground state and the barycenter of the first and second excited state, and V represents the gap between them.

important comparative values for the ZFS- and isotropic *g*-values, but not the degree of *g*-resolution needed to map the full *g*-tensor anisotropy, as is possible with the FD-FT THz-EPR method used here.

In addition, the sign of D could be deduced from analysis of the FD-FT THz-EPR spectra and VFVT curves (Figure S4). For **1**, the energy corresponding to $2E$ (the splitting between the first and the second excited state without magnetic field, Figure 1d) is larger than the thermal energy at the experimental temperature ($2E$ = 6.3 cm^{-1} corresponds to ∼9 K > 4.8 K). As the S = 1 sublevels are occupied according to Boltzmann statistics, the relative intensities of the $\Delta M_S = \pm 1$ spin transitions are very sensitive to the sign of D. For positive D (situation shown in Figure 1), both $\Delta M_S = \pm 1$ transitions from the M_S = 0 magnetic ground microstate have equal intensity. For negative D, $M_S = -1$ becomes the energetically lowest lying magnetic microstate, carrying most of the spin population. Therefore, the transition from this level to M_S = 0 would result in much more intense EPR absorption than the transitions between the nearly unoccupied excited magnetic microstates.

Typically, SOC of excited states into the ground state represents the predominant contributions to ZFS in transition-metal complexes. Hence, the observed large positive D-value for **1** indicates the presence of low-lying excited states. Furthermore, $g_\perp$, being considerably larger than g_e, signals the existence of unquenched orbital angular momentum, again arising from SOC with closely spaced excited states. Despite this, as has been shown elsewhere[34] and verified herein, a pure S = 1 SH model suffices to parametrize magnetic properties of a low-lying magnetic triplet even for those having significant unquenched orbital angular momentum. In other words, one can successfully reproduce EPR and magnetometry data using a simple SH (eq 1). Use of a more elaborate Hamiltonian that explicitly accounts for orbital angular momentum and its interactions, such as a Griffith Hamiltonian,[35] is not necessary.

Despite their usefulness for simulating EPR and SQUID data, SH models have clear limitations as they cannot usually establish a direct relationship between the magnetic properties of a complex and its electronic structure without the detour of quantum chemical calculations. This direct relationship, however, is a necessary prerequisite for a systematic investigation of the nature of the ground-level near-degeneracy via the magnetic anisotropy. To directly relate magnetic properties and electronic structure, a different EH formalism needs to be formulated. To do so, a set of states, a so-called model space, is preselected, and their energy separations are parametrized with a limited number of undetermined factors. Furthermore, one assumes that SOC and electronic Zeeman interactions involving any state out of the model space can be neglected, while exclusively those within the model space need to be considered. Hence, first wave-function-based *ab initio* computations were performed to prescreen excited states that likely make dominant contributions to the magnetic properties of the ground level of **1**. This substantially reduces the number of unknown energy gaps among them and the dimension of the resulting matrix of the EH. In this aspect, it differs from usual ligand field type analyses, which often require a large basis dimension, because of the lack of prescreening, and usually yield a range of interconnected parameters. The complexity of ligand-field models essentially foiled attempts to pinpoint key electronic-structure features that are responsible for unusual

https://doi.org/10.1021/jacsau.4c01256
JACS Au 2025, 5, 1016−1030

magnetic properties.[36] In contrast, the EH approach is well-suited for rationalizing magnetic interactions of systems featuring orbital near-degeneracy.

Calculations of the Electronic Structure of 1

As shown in Figure 2a, CASSCF(8,12)/NEVPT2 computations revealed that the ground state of **1** consists of a leading electron configuration of $(d_{x^2-y^2} + \pi_y^*)^2(d_{xy} + \pi_x^*)^2(d_{z^2})^2(d_{yz})^1(d_{xz})^1$, which accounts for 79% of the wave function. In the present case, due to the considerable π-accepting capability of the C=C moieties of dvtms, the Fe d_{xy} and $d_{x^2-y^2}$ atomic orbitals are substantially stabilized by strong π-backdonation to the formally unoccupied C=C π^* orbitals, thereby leading to two pairs of bonding and antibonding molecular orbitals denoted $d_{xy} \pm \pi_x^*$ and $d_{x^2-y^2} \pm \pi_y^*$. Such interactions are rather covalent as implied by nearly identical percentages of Fe 3d and C=C π^* contributions in $d_{xy} \pm \pi_x^*$ and $d_{x^2-y^2} \pm \pi_y^*$. While the Fe d_{z^2}, d_{xz} and d_{yz} atomic orbitals are essentially nonbonding in nature, the $3d_{z^2}$ based orbital gets somewhat stabilized because of mixing with 4s and becomes doubly occupied in the ground state.

Ab initio computations further suggest that the first and second excited states of **1** arise from single excitations from d_{z^2} to d_{yz} and to d_{xz}, and thus possess dominant electronic configurations of $(d_{x^2-y^2} + \pi_y^*)^2(d_{xy} + \pi_x^*)^2(d_{z^2})^1(d_{yz})^2(d_{xz})^1$ and $(d_{x^2-y^2} + \pi_y^*)^2(d_{xy} + \pi_x^*)^2(d_{z^2})^1(d_{yz})^1(d_{xz})^2$ (Figure 2b), respectively. The third and fourth excited states are of primary ligand-to-metal charge transfer (LMCT) character, originating from excitations from $d_{xy} + \pi_x^*$ to d_{yz} and $d_{x^2-y^2} + \pi_y^*$ to d_{yz}. As illustrated in Table S4, irrespective of the number of excited states and the spin multiplicities under investigation, CASSCF-(8,12)/NEVPT2 computations invariably deliver a low energy gap (Δ) of less than 2500 cm^{-1} and a marginal splitting $V \approx$ 200 cm^{-1} between the two excited states. The third and fourth excited states were computed to lie more than 16,000 cm^{-1} above the ground state. It should be pointed out that the computed energy gaps among the ground state and the first and second excited states fall into the uncertainty range of wave-function-based *ab initio* quantum chemical calculations and hence may not be quantitatively accurate. Despite this uncertainty, the SH parameters, D = 34.7 cm^{-1}, E/D = 0.06 cm^{-1}, g_x = 2.45, g_y = 2.40 and g_z = 1.98, predicted by the three-root computations, agree with the experimental values reasonably well, and calculations targeting an increased number of excited states do not discernibly improve the results. Remarkably, irrespective of the number of roots considered, the lowest g-value was computed to be invariably smaller than g_e (Table S4), which is rather unusual for a mononuclear transition metal complex having a more than half-filled d shell.

Effective Hamiltonian for Complexes with Near-Degenerate Ground Levels

Although CASSCF/NEVPT2 calculations reproduce the SH parameters of **1**, the underlying physical origins remain elusive and more critically, insights deduced from calculations on an individual complex hardly can be carried over to similar systems. To set up a generalized magneto-structural correlation, an EH is derived to explicitly consider the SOC and the electron Zeeman interaction in the basis of the low-lying electronic triplet as suggested by *ab initio* computations (Figure 2b). For V = 0, the system has effective D_3 symmetry, and states $^3A_{2g}$, $^3E_g(x)$ and $^3E_g(y)$ can be readily distinguished. To be consistent, even for $V \neq 0$ the same labels will be used. Therefore, the EH operator, $\hat{H}_{EH}$, consists of three terms (eqs 2a−2c)

$$\hat{H}_{EH} = \hat{H}_{\Delta} + \hat{H}_{SOC} + \hat{H}_{Zee} \tag{2a}$$

$$\hat{H}_{SOC} = \zeta \sum_n \sum_{k=x,y,z} \hat{l}_k(n)\cdot\hat{s}_k(n) \tag{2b}$$

$$\hat{H}_{Zee} = \sum_n \mu_B[\hat{l}(n) + g_e\hat{s}(n)]\cdot\boldsymbol{B_0} \tag{2c}$$

$\hat{H}_{\Delta}$ is the unperturbed nonrelativistic energy gap between $^3A_{2g}$ and $^3E_g(x)$ and $^3E_g(y)$ in the Born−Oppenheimer Hamiltonian. $\hat{H}_{SOC}$ and $\hat{H}_{Zee}$ account for SOC and Zeeman interactions, including spin and orbital Zeeman terms. ζ = 320 cm^{-1} is the effective SOC constant of Fe(0) obtained from earlier calculations.[37]

The EH is constructed in the basis of the low-lying electronic triplet by utilizing their many-electron basis functions in terms of normalized Slater determinants. For M_S = +1, the many-electron basis functions are given by (eqs S1a-i)

$$|^3A_{2g}, +1\rangle = |d_{z^2}\,\overline{d}_{z^2}d_{yz}d_{xz}| \tag{3a}$$

$$|^3E_g(x), +1\rangle = |d_{z^2}d_{yz}\,\overline{d}_{yz}d_{xz}| \tag{3b}$$

$$|^3E_g(y), +1\rangle = |d_{z^2}d_{yz}d_{xz}\,\overline{d}_{xz}| \tag{3c}$$

A bar (no bar) on top of a given orbital indicates that this orbital is occupied by a spin-down (spin-up) electron. The filled $d_{xy} + \pi_x^*$ and $d_{x^2-y^2} + \pi_y^*$ orbitals are excluded because the associated excited states, according to the above CASSCF-(8,12)/NEVPT2 calculations, lie more than 16,000 cm^{-1} above the ground state. The nonvanishing matrix elements of $\hat{H}_{\Delta}$ are given by

$$\langle^3E_g(x), M_S|H_{\Delta}|^3E_g(x), M_S\rangle = \Delta + V/2 \tag{4a}$$

$$\langle^3E_g(y), M_S|H_{\Delta}|^3E_g(y), M_S\rangle = \Delta - V/2 \tag{4b}$$

Shown in Table S2 is the EH matrix in the basis of the nine magnetic sublevels of $^3A_{2g}$, $^3E_g(x)$ and $^3E_g(y)$. To treat the SOC and the electron Zeeman splitting of the magnetic microstates derived from $^3A_{2g}$, $^3E_g(x)$ and $^3E_g(y)$ on the same footing as their energy separations, we did not employ second-order perturbation theory, but diagonalized the EH matrix, which amounts to infinite order perturbation treatments. Thereby, the wave-functions of the three low-lying magnetic levels, $|\varphi_i\rangle$ (i = 1, 2, 3), and their energies at zero field and the variations thereof in the presence of a magnetic field were readily obtained. Furthermore, all SH parameters can be directly extracted. (For details, please refer to the SI). As elaborated in the following, the EH analyses predict D = 33.97 cm^{-1}, E = 3.33 cm^{-1}, g_x = 2.423, g_y = 2.509 and g_z = 1.977, alongside Δ = ≈ 1800 cm^{-1} and V = ≈300 cm^{-1}. As such, the obtained SH parameters are all in very reasonable agreement with experiment, and the energy gaps between the unperturbed electronic triplets are close to those estimated by *ab initio* CASSCF(8,12)/NEVPT2 computations.

The SH parameters determined experimentally indicate that complex **1** features a pseudoaxial symmetry as evidenced by a small E/D value of ∼0.1. To simplify our analyses and gain a better understanding of the physical origin of the magnetic anisotropy measured for **1**, we first assumed effective D_3

https://doi.org/10.1021/jacsau.4c01256
JACS Au 2025, 5, 1016−1030

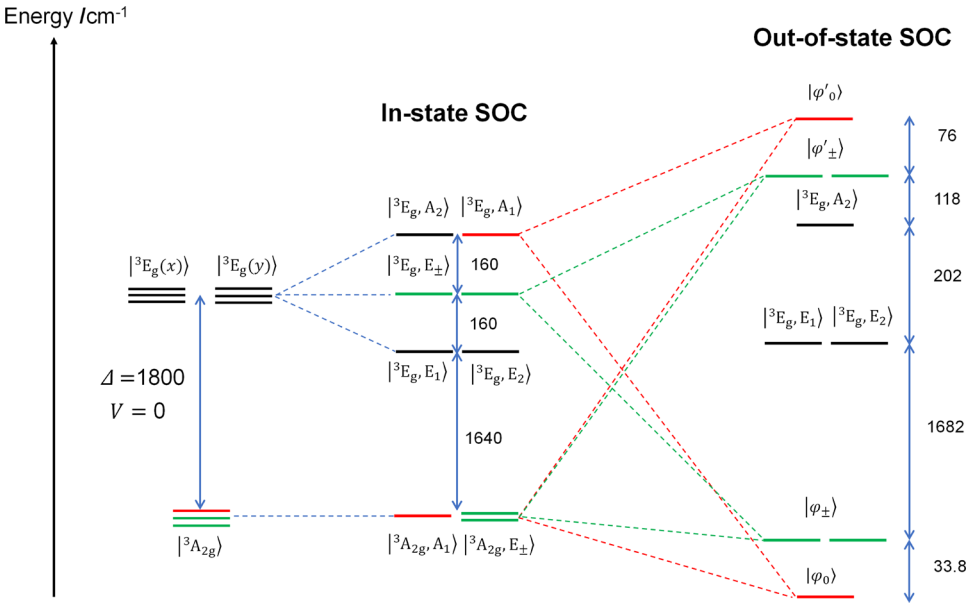

Figure 3. Energy spectra considering no SOC (left), in-state SOC (middle) and out-of-state SOC (right) with ζ = 320 cm^{-1}, Δ = 1800 cm^{-1} and V = 0 cm^{-1} (see eqs 4a, 4b and Figure 2 for the definition of Δ and V). In-state SOC considers only the interactions among components of the same irreducible representation, i.e. the two components of ^3E_g, and out-of-state SOC deals with all SOC interactions between $^3A_{2g}$ and ^3E_g (eqs 3a−3c). Magnetic microstates resulting from in-state SOC of ^3E_g are labeled $|^{2S+1}\Gamma_1, \Gamma_2\rangle$, where Γ_1 and Γ_2 are the irreducible representations of D_3 and its double group (see eqs S11−S13 in the SI), respectively. Dotted red and green lines represent the two distinct channels of out-of-state SOC between $^3A_{2g}$ and ^3E_g, respectively. $|\varphi_0\rangle$,$|\varphi'_0\rangle$,$|\varphi_\pm\rangle$,$|\varphi'_\pm\rangle$ (eqs 7a−7c) represent the six magnetic sublevels arising from the out-of-state SOC. Those magnetic sublevels displayed in black are unaffected by the out-of-state SOC.

symmetry and then considered the effect of orthorhombic distortion V afterward. As shown in Figure 3, when $^3E_g(x)$ and $^3E_g(y)$ are exactly degenerate, as elaborated in our earlier work,[8] the first-order SOC, so-called in-state SOC, restores orbital angular momentum along the z-direction, and splits the ^3E_g state into three accidentally degenerate doublets. The second-order SOC, often referred to as out-of-state SOC between the $^3A_{2g}$ and ^3E_g states, lifts the two-fold degeneracy of the first, third and fourth doublets. In the absence of an external magnetic field, diagonalizing the $\boldsymbol{H}_\Delta$ and $\boldsymbol{H}_{SOC}$ parts of the EH matrix yields the wave functions of the nine magnetic sublevels. Of them, the lowest-energy one, denoted $|\varphi_0\rangle$, is nondegenerate, and two degenerate microstates, denoted $|\varphi_\pm\rangle$, are the next higher ones in energy (Figure 3).

As such, the situation corresponds to a fictitious $\tilde{S}$ = 1 spin system ($|1,M_S\rangle$, M_S = 0, ± 1) with easy-plane magnetization in the SH formalism, and $|\varphi_0\rangle$ and $|\varphi_\pm\rangle$ are hence equivalent to $|1,0\rangle$ and $|1, \pm1\rangle$, respectively. Therefore, the axial ZFS parameter, D, is simply the energy difference between $|\varphi_0\rangle$ and $|\varphi_\pm\rangle$

$$D = E(|\varphi_\pm\rangle) - E(|\varphi_0\rangle) \tag{5}$$

Analogously, the g-values can be computed as follows[8,34]

$$g_\parallel = |\langle\varphi_+|2\hat{S}_z + \hat{L}_z|\varphi_+\rangle| \tag{6a}$$

$$g_\perp = \sqrt{2}\,|\langle\varphi_0|2\hat{S}_x + \hat{L}_x|\varphi_+\rangle| \tag{6b}$$

Figure 4 shows the SH parameters, D, $g_\parallel$ and $g_\perp$ computed as a function of Δ. At $\Delta = 5.6\zeta$ = 1800 cm^{-1}, the best match between the calculated and the experimental D-values was achieved. With this Δ-value, we examined the state composition of the nine magnetic sublevels and dissected the physical origins of the magnetic anisotropy. Because out-of-

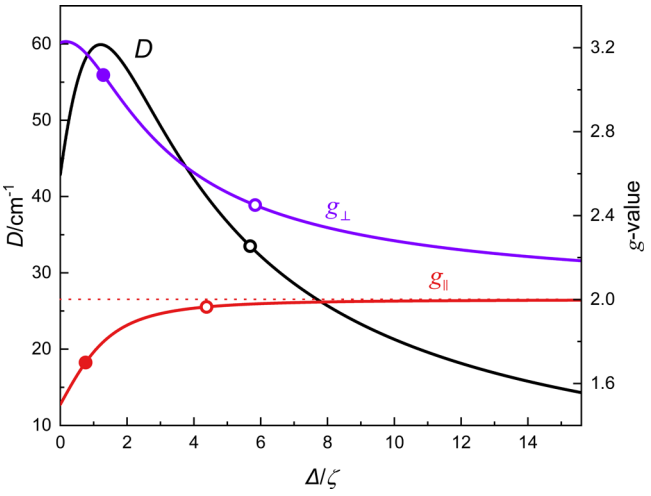

Figure 4. Calculated D (black), $g_\parallel$ (red) and $g_\perp$ (purple) plotted vs Δ/ζ (see eqs 5, 6a and 6b, respectively). The open circles indicate the experimental SH parameters for complex **1** determined from THz-EPR (Table S1), while the closed circles represent the experimental g-values of **3** reported in ref 8.

state SOC admixes ^3E_g into $^3A_{2g}$, the wave functions of the final low-lying magnetic triplet are given by the following expressions:

$$|\varphi_0\rangle = -0.982i|^3A_{2g}, A_1\rangle - 0.189|^3E_g, A_1\rangle \tag{7a}$$

$$|\varphi_+\rangle = -0.989|^3A_{2g}, E_+\rangle + 0.149i|^3E_g, E_+\rangle \tag{7b}$$

$$|\varphi_-\rangle = +0.989i|^3A_{2g}, E_-\rangle - 0.149|^3E_g, E_-\rangle \tag{7c}$$

Therefore, $|\varphi_0\rangle$, and $|\varphi_\pm\rangle$ contain 4% and 2% contribution of $|^3E_g, A_1\rangle$ and $|^3E_g, E_\pm\rangle$, respectively (compare Figure 3), and

https://doi.org/10.1021/jacsau.4c01256
JACS Au 2025, 5, 1016−1030

those minor, yet discernible parentages of ^3E_g in the low-lying magnetic triplet suggest that the symmetrized complex **1** features a nearly triply degenerate ground level.

Figure 5 depicts the spin ($g_{S,\parallel}$ and $g_{S,\perp}$) and orbital ($g_{L,\parallel}$ and $g_{L,\perp}$) contributions to $g_\parallel$ and $g_\perp$ as a function of Δ derived from EH analyses (solid lines) and second order perturbation theory (dotted lines), respectively. Apparently, $g_\parallel$ and $g_\perp$ estimated by second-order perturbation theory exceed the values calculated by EH analysis. Second-order perturbation theory predicts that a single-electron excitation from a doubly to a singly occupied orbital, like in the case of **1** (see Figure S10), leads to *g*-values equal or larger than g_e. This contrasts our experimental findings, which are in line with the predictions from the EH analysis (see Figure 4).

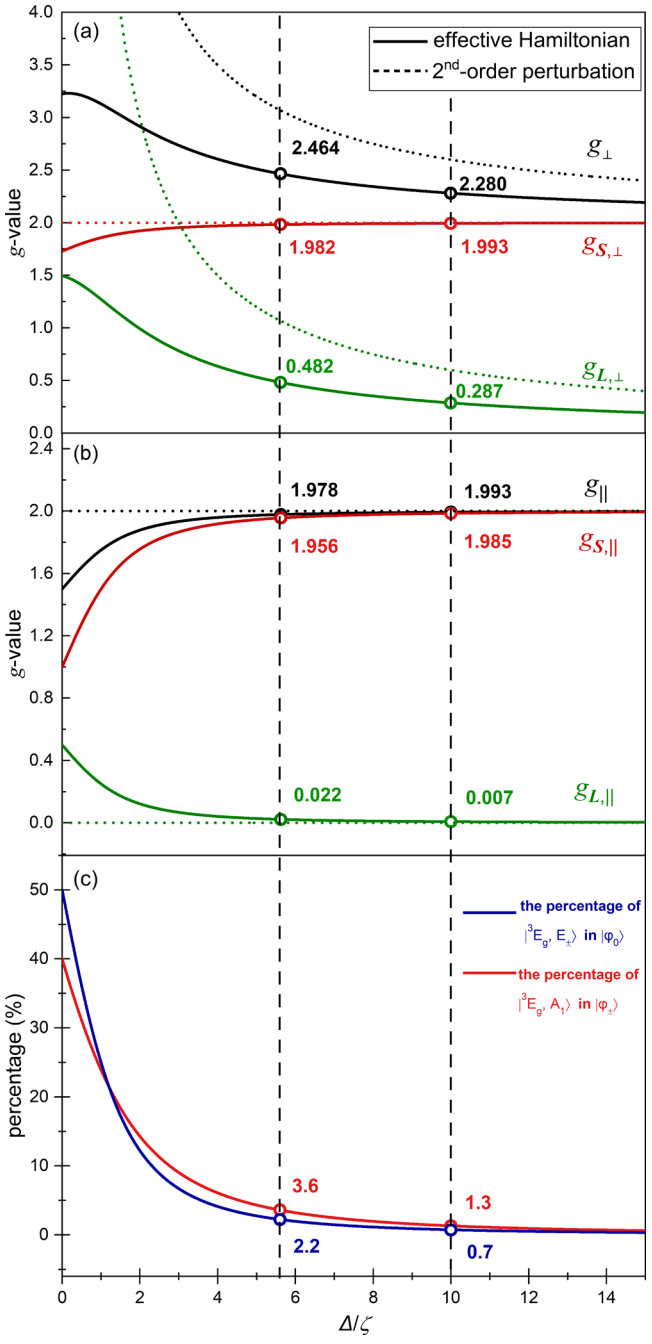

Figure 5. Variation of (a) $g_{S,\perp}$, $g_{L,\perp}$, $g_\perp$, (eqs 6b, 8c and 8d, respectively) (b) $g_{S,\parallel}$, $g_{L,\parallel}$, $g_\parallel$, (eqs 6a, 8a and 8b, respectively) and (c) the respective percentages of $|^3E_g, E_\pm\rangle$ in $|\varphi_0\rangle$ and $|^3E_g, A_1\rangle$ in $|\varphi_\pm\rangle$ as a function of Δ/ζ, derived from EH analysis (solid lines). Dotted lines represent *g*-values computed by second-order perturbation theory. Dashed vertical lines indicate the corresponding values calculated for complex **1** with $\Delta = 5.6\zeta = 1800\ cm^{-1}$ and for systems with $\Delta/\zeta = 10$, respectively.

$$g_{S,\parallel} = |\langle\varphi_+|2\hat{S}_z|\varphi_+\rangle| \tag{8a}$$

$$g_{L,\parallel} = |\langle\varphi_+|\hat{L}_z|\varphi_+\rangle| \tag{8b}$$

$$g_{S,\perp} = \sqrt{2}\,|\langle\varphi_0|2\hat{S}_x|\varphi_+\rangle| \tag{8c}$$

$$g_{L,\perp} = \sqrt{2}\,|\langle\varphi_0|\hat{L}_x|\varphi_+\rangle| \tag{8d}$$

As can be seen from Figure 5, $g_{L,\perp}$ rises dramatically with decreasing Δ, which originates from the SOC of ^3E_g and $^3A_{2g}$, introducing substantial unquenched transverse orbital angular momentum into the low-lying magnetic triplet. For the same reason, $g_{L,\parallel}$ completely arises from the orbital angular momentum of the minor contribution of $|^3E_g, E_+\rangle$ to $|\varphi_+\rangle$, a third-order term in the perturbative treatment of *g*-shifts.

Unexpectedly, the EH analyses reveal that in the presence of strong SOC both $g_{S,\parallel}$ and $g_{S,\perp}$ are considerably lower than g_e, indicating that SOC can quench the spin angular momentum in all directions. In the present case, $g_{S,\parallel}$ entirely stems from the spin angular momentum of the leading component $|^3A_{2g}, E_+\rangle$ in $|\varphi_+\rangle$, because, as elaborated in SI eqs S11e−S12g, $|^3E_g, E_+\rangle$ has a lower eigenvalue of 0 with respect to $\hat{S}_z$, viz. $\langle\hat{S}_z\rangle = 0$, than $|^3A_{2g}, E_+\rangle$, which is distinguished by $\langle\hat{S}_z\rangle = 1$. Therefore, the SOC-induced state admixing of $|^3E_g, E_+\rangle$ into $|^3A_{2g}, E_+\rangle$ dilutes the spin angular momentum of the latter. The same dilution effect also accounts for $g_{S,\perp}$ being lower than g_e. Furthermore, $|^3A_{2g}, E_+\rangle$ and $|^3E_g, E_+\rangle$ are the eigenfunctions of $\hat{L}_z$ with eigenvalues of 0 and +1, respectively, but since g_e of the spin angular momentum is just twice of that of the orbital angular momentum (which is 1), the decrement of the spin contribution to $g_\parallel$ due to the mixing of $|^3E_g, E_+\rangle$ in $|\varphi_+\rangle$ exceeds its orbital contribution. As such, $g_\parallel$ is less than g_e. Finally, as Δ/ζ decreases from 15 to 0, the weight of $|^3E_g, E_+\rangle$ in $|\varphi_+\rangle$ increases, and $g_\parallel$ steadily declines from 2 to 1.5. On the contrary, $g_\perp$ is always significantly larger than g_e, because $g_{L,\perp}$ is invariably in excess of the difference of $g_{S,\perp}$ relative to g_e.

As depicted in Figure 5c, when $\Delta/\zeta > 10$, the mixing between $|^3E_g\rangle$ and $|^3A_{2g}\rangle$ caused by SOC is negligible with minor percentages of $|^3E_g, E_\pm\rangle$ and $|^3E_g, A_1\rangle$ in $|\varphi_0\rangle$ and $|\varphi_\pm\rangle$ being 1.3 and 0.7%, respectively, and so is the quenching of the spin angular momentum of $|^3A_{2g}\rangle$; therefore, $2 = g_\parallel < g_\perp$, congruent with the *g*-value pattern predicted by perturbation theory. Therefore, $\Delta/\zeta = 10$ can be viewed as the turning point where the perturbation treatment on the low-lying electronic triplet breaks down. Because $g_\parallel$ is essentially 2 for Δ/ζ in the range of 8−12, the choice of $\Delta/\zeta = 10$ as the cutoff to differentiate between systems having nondegenerate or near-degenerate ground levels is somehow arbitrary. But in any case, as the energy splitting of the near-degenerate states declines, the SOC-induced quenching of the spin angular momentum gets increasingly pronounced and hence should be regarded as a more appropriate hallmark to identify whether systems have near-degenerate ground levels or not. Following this line of reasoning, complexes with nearly triple or double degenerate ground levels ought to be distinguished by one or two *g*-values,

https://doi.org/10.1021/jacsau.4c01256
JACS Au 2025, 5, 1016−1030

respectively, smaller than g_e in the directions where orbital angular momentum is almost quenched.

We are now in a position to examine the influence of the rhombic splitting V between $^3E_g(x)$ and $^3E_g(y)$ on the magnetic properties of **1**. Starting from $V = 0$ in Figure 6,

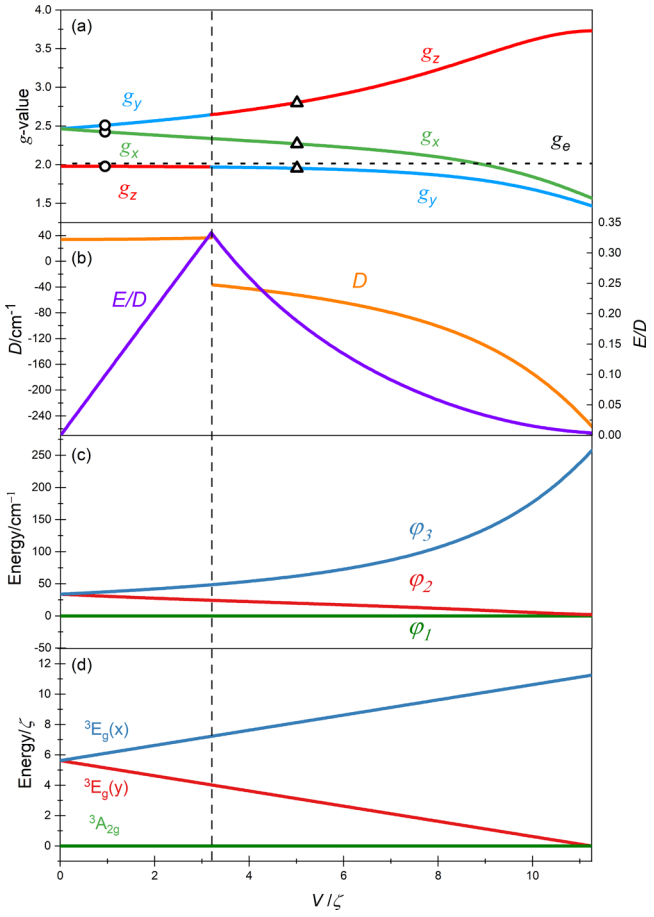

Figure 6. V/ζ, dependence of (a) g_x (green), g_y (blue) and g_z (red), (b) the ZFS-values D (orange) and E/D (purple), (c) the three low-lying microstates $|\varphi_i\rangle$ (i = 1, 2 and 3) (green, red and blue) (see eqs S2a–c and Table S2) and (d) the low-lying electronic triplets (see Figure 2b) $^3A_{2g}$ (green), $^3E_g(x)$ (blue) and $^3E_g(y)$ (red). All parameters were calculated for fixed $\Delta = 5.6\zeta = 1800$ cm^{-1} with $\zeta = 320$ cm^{-1} (see Figure S7 for further calculations with varying Δ). The black open circles and triangles represent the situations for **1** with $V = 0.94\zeta = 300$ cm^{-1} and for complex **6** with $V = 5\zeta = 2450$ cm^{-1}, respectively. The black dashed line indicates the situation where the three lowest states $|\varphi_i\rangle$ have equal energy spacing and $E/D = 1/3$.

where $g_z = g_\parallel < 2 < g_\perp = g_x = g_y$, with increasing V, g_x declines and g_y rises to $g_z < 2 < g_x < g_y$, which mirrors the energy variations of $^3E_g(x)$ and $^3E_g(y)$. While increasing V from 0, the D-value is essentially unchanged, but E/D increases sharply. Remarkably, at $V = 3.19\zeta = 1020$ cm^{-1} (black dashed line in Figure 6), the sign of D switches from positive to negative, while E/D reaches the maximum value of 1/3. When E/D is close to 1/3, the two energy gaps of the three low-lying magnetic sublevels are nearly identical and one can map the lowest-energy one, $|\varphi_0\rangle$, either to $M_S = 0$ or to $M_S = -1$. As a result, when $V > 3.19\zeta$, the sign of D changes, and the principal z-axis of the traceless ***D***-tensor transitions from the molecular z-axis to the y-axis. In experiments, the principal axes of the ***g***-tensor are typically referenced to those of the ***D***-tensor, the three g-values are thus relabeled accordingly as $g_y < 2 < g_x \ll g_z$ in Figure 6. As V further increases, the energy gap between $^3A_{2g}$ and $^3E_g(x)$ substantially exceeds that between $^3A_{2g}$ and $^3E_g(y)$; consequently, g_x changes from being higher than g_e to being lower than g_e, resulting in a g-value pattern of $g_x \approx g_y < 2 \ll g_z$. At the same time, the magnitude of the negative D-value constantly ascends, while E/D reduces. Ultimately, the system is best formulated as having two-fold pseudodegeneracy, as manifested by $D \ll 0$ and $g_x \approx g_y = g_\perp < 2 \ll g_z = g_\parallel$, even as the energy separations within the low-lying electronic triplet remain below 10ζ. Accordingly, for a $(d_{z^2}d_{xz}d_{yz})^4$ $S = 1$ system with three orbital states lying in an energy range of less than 10ζ, three different scenarios with characteristic magnetic anisotropies can be envisioned (see discussion above and Figure S10).

As shown in Figure 7, first, type I triple near-degeneracy, where the energy gap of the upper two states is negligible compared to their energy difference with respect to the lower state. Second, type II triple near-degenerate levels, with considerable rhombic splitting lifting the quasi-degeneracy of the upper two states and resulting in three nearly equally spaced energy states. Finally, doubly near-degenerate levels have two very close lying states and a third energetically much higher lying state.

To generalize this classification, we explored more situations varying Δ from ζ to 9ζ. As shown in Figure S7, the transition point between type I and II triple near-degeneracy, distinguished to be $E/D = 1/3$, is in a narrow range from $V/\Delta = 0.5$ to 0.6 upon increasing Δ. However, the boundary between type II triple near-degeneracy and double near-degeneracy depends heavily on Δ. For $\Delta < 1.25\zeta$, $V/\Delta < 2$ does not allow the existence of double degeneracy. More important is that in the double degenerate regime, the system invariably exhibits the characteristic EPR signature of $g_z > 2 > g_{x,y}$ and $D \ll 0$, even if the second orbital excited state is situated by less than 10ζ in energy relative to the ground one. As such, one can determine whether one or two excited states dominate the SOC interaction, even for cases where more than three low-lying excited states exist.

Comparison to other Low-Coordinate Complexes

In the following, magneto-structural correlations derived for complex **1** are compared to related three-coordinate complexes shown in Chart 1. Complexes **4** and **4′** have $D = +16.8$ cm^{-1} and $E/D = 0.2$ and $D = +14.3$ cm^{-1} and $E/D = 0.26$, respectively. On the contrary, complex **5** exhibits $D = -20$ cm^{-1} and $E/D = 0.2$, despite sharing an analogous geometric structure to **4** and **4′**. Based on the following detailed ligand field analysis of their electronic structures, we reasoned that these three complexes may all possess near-degenerate ground levels as reflected by their appreciable D-values, and specifically be in the intermediate region between type I and II triple near-degeneracy as suggested by their sizable E/D-values (see black dashed line in Figure 6).

In analogy to the bonding situation of **1**, the strong σ donation of the supporting ligands in **4**, **4′** and **5** raises the $d_{x^2-y^2}$ and d_{xy} orbitals to higher energies, and the remaining d_{z^2}, d_{yz} and d_{xz} orbitals are nearly nonbonding (Figure 8). However, in the case of complex **5**, the d_{yz} orbital gets somewhat stabilized, because of its π back-bonding interaction with the NHC π^* orbital. Consequently, the energy separation between the d_{z^2} and d_{yz} orbitals shrinks, and complex **5** is best interpreted as possessing a type II triply degenerate ground

https://doi.org/10.1021/jacsau.4c01256
JACS Au 2025, 5, 1016−1030

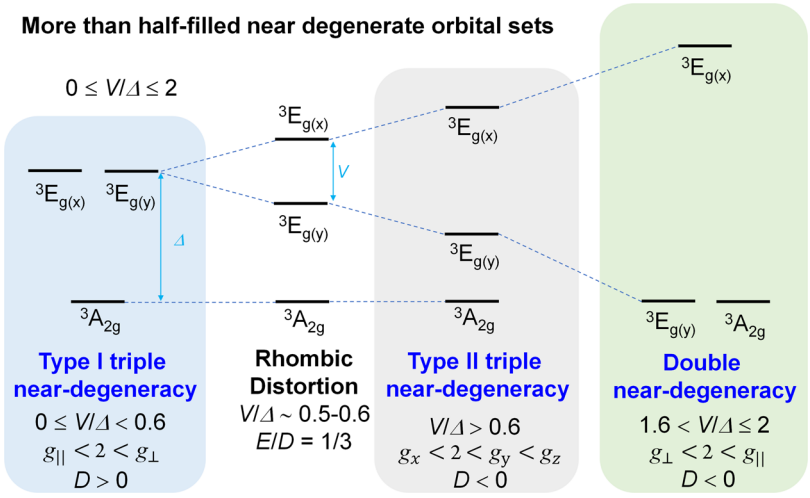

Figure 7. Electronic-structure scenarios for a $(d_{z^2}d_{xz}d_{yz})^4$ $S = 1$ system having three low-lying orbital states. Type I and II triple degeneracy are separated by the configuration where the ZFS tensor reaches its maximum rhombicity.

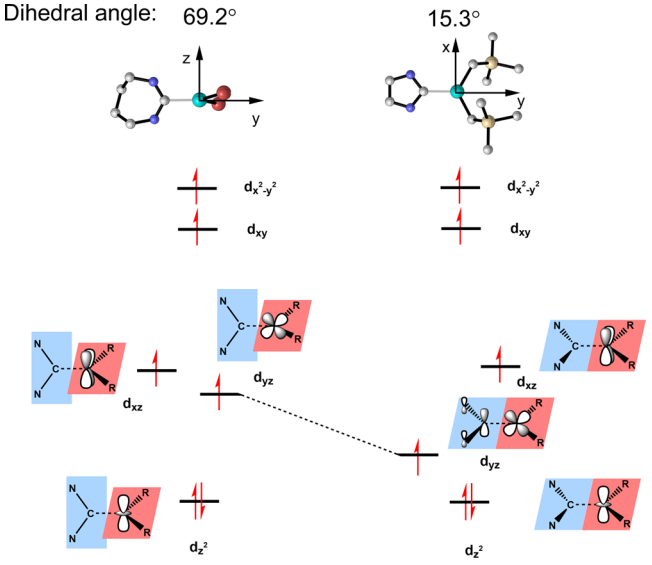

Figure 8. Geometric and electronic structure of **4** and **5**. The dihedral angles formed between the R-Fe-R (R = Br^- and CH_2TMS^-) plane and the plane of the carbene N−C−N-plane are 65.4 and 15.3° in complexes **4** and **5**, respectively. All carbene substituents are omitted for clarity.

level, in accordance with its negative D. In contrast, for complexes **4** and **4′**, the corresponding π back-bonding interaction is much weaker, because of an unfavorable geometry with a much larger dihedral angle of 69.2 and 86.8°, respectively, between the R-Fe-R (R = Br^-) plane and the carbene N−C−N plane. Therefore, the ground levels of complexes **4** and **4′** still feature type I triple near-degeneracy consistent with their positive D-values.

CASSCF(6,10)/NEVPT2 calculations substantiate the views deduced from the ligand field analysis. As shown in Table S5 and Figures S8 and S9, the greatest energy separations within the low-lying electronic triplets of complexes **4** and **5** were predicted to be less than 2400 cm^{-1}, indicating that both species possess near-degenerate ground levels. Specifically, the ground level of **4** features type I triple degeneracy as suggested by $V/\Delta = 0.65$, consistent with its positive D-value. In the case of **5**, because of the π back-bonding interaction between the NHC π^* and Fe d_{yz} orbitals, the second excited state has a much lower energy than the third one. Consequently, complex **5** has a type II triply near-degenerate ground level with V/Δ = 1.3, congruent with its negative D-value and reduced rhombicity as compared to **4**.

Recently, some of us reported that an $S = 1$ three-coordinate Fe(IV) bisimido complex $[(IPr)Fe^{IV}(NC(CF_3)_2Ph)_2]$ (**6**)[38] has an orbitally nearly doubly degenerate ground level. This electronic structure description is congruent with its strong easy-axis magnetization with $D = -79.2$ cm^{-1}, $E/D = 0.09$, $g_{\|} \approx 2.80$ and $g_{\perp} = 1.83$, revealed by SQUID magnetometry and applied field Mössbauer spectroscopy. Furthermore, wave-function-based *ab initio* calculations predicted that the dominant ground electron configuration $(d_{z^2})^2(d_{yz})^1(d_{xz})^1$ is only 1020 cm^{-1} lower in energy than the first excited state $(d_{z^2})^1(d_{yz})^2(d_{xz})^1$. The bonding situation of complex **6** is thus analogous to that of **1** except that the two spectator orbitals, $d_{x^2-y^2}$ and d_{xy} are empty in the former. The EH model is therefore applicable to **6** by setting the following parameters to match the largest g-value determined experimentally (open triangles in Figure 6a): the effective one-electron SOC constant of Fe(IV) ζ = 487 cm^{-1}, $\Delta = 5.6\zeta$, $V/\Delta = 0.89$. The resulting EH gives $D = -81.0$ cm^{-1}, $E/D = 0.18$ and $g_z = 2.81$, $g_x = 2.26$ and $g_y = 1.95$. Given the fact that $g_{x,y}$ cannot be accurately determined by experimental spectroscopic characterizations, all values are in reasonable agreement with the experiment, although the simple EH model makes crude approximations, such as neglecting the metal−ligand covalency.

Early work by Holland, Münck, Bominaar and co-worker delineates an electron structure analysis of a series of high-spin ($S = 2$) three-coordinate Fe(II) complexes $[LFe^{II}Cl]$ (**2′**, L = β-diketiminate) and $[LFe^{II}CH_3]$ (**2**) with applied-field Mössbauer and parallel-mode EPR spectroscopies.[39] It has been concluded that they possess orbitally almost doubly degenerate ground levels in concert with their large negative D-values ($|D| > 50$ cm^{-1}) and unusual effective $g'_z = 10.9$ (**2**) and $g'_z = 11.4$ (**2′**) along the z-direction of the $\boldsymbol{D}$-tensor. The effective g'-values are obtained by mapping the lowest-energy $M_S = \pm 2$ pseudodoublet of an $S = 2$ multiplet to $M_S = \pm 1/2$ of an effective $S = 1/2$ doublet. Hence, the intrinsic g_z-values

https://doi.org/10.1021/jacsau.4c01256
JACS Au 2025, 5, 1016−1030

are 2.73 for **2** and 2.85 for **2′** because of the vanishing rhombicity, $E/D \approx 0$.

Very recently, Telser, Holland and co-workers provided more accurate D-values for **2** (−38.1 cm^{-1}) and **2′** (−36.9 cm^{-1}) measured by frequency-domain far-infrared magnetic resonance spectroscopy (FIRMS) and confirmed their strong easy-axis magnetic anisotropy.[40] By contrast, as to the $S = 3/2$ Co^{II} congeners, [$LCo^{II}Cl$] (**7**) was found to feature strong easy-plane magnetic anisotropy as manifested by $D = +55$ cm^{-1}, alongside effective $g'_x = 4.60$, $g'_y = 5.64$ and $g'_z = 1.97$, whereas [$LCo^{II}CH_3$] (**7′**) was characterized as having $D = -49$ cm^{-1} and $g'_z = 8.50$. For complexes **7** and **7′**, E/D are very low and cannot be precisely determined. If E/D is assumed to be zero, then the effective g'-values can be converted to the intrinsic g-values as follows, $g_\perp \approx 2.56$ and $g_\parallel = 1.97$ for **7** and $g_\parallel \approx 2.83$ for **7′**.

Ab initio calculations revealed that three low-lying excited states exist above the ground state within an energy gap of 2000 cm^{-1}, arising from closely spaced d_{z^2}, d_{xz} and d_{yz} orbitals.[40] Despite this complexity, **7′** was computed to possess a doubly near-degenerate ground level, consistent with the measured D- and g-values, while **7** has type I triple near-degeneracy, also in line with the EPR findings. The difference can be traced back to the fact that a methyl group is a pure σ donor, but chloride is a σ and π donor. This disparate property of the axial ligands changes the energy of d_{yz} relative to d_{z^2} and causes the varying degrees of orbital near-degeneracy as proposed by Telser, Holland and co-workers (see the Supporting Information in ref 40). These two examples support our conclusion that the g-anisotropy and the sign of D can be used to determine the number of lowest-energy orbital excited states that strongly interact with the ground state via SOC even for those difficult cases where a range of low-lying excited states exist.

General Criteria to Identify the Degree of Ground-Level Near-Degeneracy from *g*- and ZFS-Values

Up to here, we have established a magneto-structural correlation for three-coordinate systems. In the following, we generalize our above EH analysis and propose criteria to identify the degree of ground-level near-degeneracy (Table 1).

Table 1. Criteria for the Assignment of Type I and II Triply and Doubly Near-Degenerate Ground States by Their Magnetic Anisotropy

	more than half-filled orbital sets	less than half-filled orbital sets
type I triple degeneracy	$g_\parallel < 2 < g_\perp$, $D > 0$	$g_\perp < g_\parallel < 2$ D, > 0
type II triple degeneracy	$g_x < 2 < g_y < g_z$, $D < 0$	$g_z < g_y < g_x < 2$, $D < 0$
double degeneracy	$g_\perp < 2 < g_\parallel$, $D < 0$	$g_\parallel < g_\perp < 0$, $D < 0$

For complexes having more than half-filled degenerate shells, the spin and orbital angular momenta in the low-lying magnetic sublevels orient roughly along the same direction as implied by Hund's third rule, which provides a rationale for the g-shift predicted by second-order perturbation theory (see discussion above and Figure S10). As a consequence, the g-value along the direction of the SOC interaction should be larger than g_e. Whereas due to SOC-induced state mixing, the other g-components should be less than g_e. Hence, type I triply and doubly near-degenerate systems feature distinct g-tensor anisotropy, namely $g_\perp < 2 < g_\parallel$ ($g_{x,y} < 2 < g_z$) and $g_\parallel < 2 < g_\perp$ ($g_z < 2 < g_{x,y}$), respectively. In between these two limiting situations, type II triply near-degenerate systems are likely distinguished by $g_x < 2 < g_y < g_z$. By contrast, in the case of complexes having less than half-filled degenerate orbitals, the spin and orbital angular momenta in the low-lying magnetic sublevels align approximately along the opposite direction. Therefore, g-tensor anisotropies of $g_\perp < g_\parallel < 2$ ($g_{x,y} < g_z < 2$), $g_z < g_y < g_x < 2$ and $g_\parallel < g_\perp < 2$ ($g_z < g_{x,y} < 2$) can be regarded as spectroscopic markers for type I and type II triply, and doubly near-degenerate systems, respectively. Furthermore, systematic EH analyses validated by experimental findings reveal that type I triply near-degenerate systems invariably feature positive D-values, whereas type II triply and doubly degenerate systems exhibit negative D-values. As classical examples of the latter situation, the (quasi-)linear coordination environment of Fe(I/II)[12] and Co(I/II)[13] complexes renders 3d orbitals of π or δ symmetry essentially nonbonding in nature; consequently, these systems were unanimously found to feature strong easy-axis magnetic anisotropy.

For systems having less than half-filled degenerate orbital sets and featuring two-fold pseudodegeneracy, $S = 1/2$ tetragonal iron(V)-nitrido complexes serve as good examples. Independent of their supporting ligands, these species are invariably distinguished by $g_\parallel \approx 1$ and $g_\perp \approx 1.73$, because their sole unpaired electron populates doubly near-degenerate Fe−N π^* orbitals and their ground levels possess two-fold near-degeneracy.[41] Very recently, some of us reported EPR characterizations of monosubstituted Sn(I) and Pb(I) doublet radicals. The same g-tensor patterns with g = [1.957, 1.896, 1.578] for Sn(I) and g = [1.496, 1.166, 0.683] for Pb(I) were detected.[42] The observed g-anisotropies are a consequence of their nearly doubly degenerate ground levels with an unpaired electron distributed between almost degenerate nonbonding valence p_x and p_y orbitals.

For systems having more than half-filled degenerate orbital sets and featuring type I triple degeneracy, previous work of ours[8] unequivocally established that the square-planar $S = 1$ Fe(II) porphyrin complex [Fe^{II}(TPP)] (**3**) possesses a predominant electron configuration of $(d_{xy})^2(d_{z^2})^2(d_{xz})^1(d_{yz})^1$, which lies slightly below $(d_{xy})^2(d_{z^2})^1(d_{xz/yz})^3$ by 950 cm^{-1} because in square-planar coordination arrangements, d_{z^2}, d_{xz} and d_{yz} are all essentially nonbonding in nature and hence almost energetically degenerate. This peculiar electronic structure is manifested by $g_\parallel = 1.70$, $g_\perp = 3.07$ and $D = +94$ cm^{-1} (filled circles in Figure 4) and key to its superior electrochemical activity toward CO_2 catalytic reduction. The experimental D-value of **3** exceeds that predicted by the EH for complex **1**, simply because D is not proportional to ζ but to ζ^2. Similarly, its $S = 1/2$ Co(II) analog, [Co^{II}(*p*-OCH_3)(TPP)] (**8**), also features a type I triply degenerate ground level as implied by $g_\parallel = 1.80$ and $g_\perp = 3.32$.[43] For **8**, the lowest-energy electron configuration was found to be $(d_{xy})^2(d_{xz/yz})^4(d_{z^2})^1$, which is close in energy to the doubly degenerate $(d_{xy})^2(d_{xz/yz})^3(d_{z^2})^2$. The same holds true for [Rh^{II}(TMP)] (**9**, TMP = meso-tetramesitylporphyrin) with $g_\parallel = 1.92$ and $g_\perp = 2.65$. Raising the energy of the d_{z^2} orbital in **8** and **9** by axial coordination with pyridine, CO and other ligands lifts the three-fold near-degeneracy and renders $g_\perp$ steadily approaching 2.0, depending on the σ-donating strength of the ligand.[44] For example, the five-coordinate pyridine and CO adducts of **8** were distinguished by $g_\parallel = 2.02$ and $g_\perp = 2.32$, and $g_\parallel = 2.02$ and $g_\perp = 2.24$, respectively.[43] Similarly, the triethylamine and

https://doi.org/10.1021/jacsau.4c01256
JACS Au 2025, 5, 1016−1030

isocyanide adducts of **9** exhibit $g_{\parallel}$ = 1.97 and $g_{\perp}$ = 2.39, and $g_{\parallel}$ = 2.00 and $g_{\perp}$ = 2.16, respectively.[44]

CONCLUSIONS

Herein, general relationships between the magnetic anisotropy (parametrized by the *g*- and ZFS-values) and the degeneracy of the orbital ground levels of three-coordinate transition metal complexes are established. Starting point is a precise determination of the *g*- and ZFS-values of the triplet state of complex **1**. Complementary SQUID magnetometry and FD-FT-THz-EPR spectroscopy reveal D = +33.54 cm^{-1}, E = 3.15 cm^{-1} (E/D = 0.09), $g_z = g_{\parallel}$ = 1.96 and $g_x = g_y = g_{\perp}$ = 2.45. By coupling an EH analysis with wave-function-based CASSCF/NEVPT2 calculations, we show that the pronounced magnetic easy-plane anisotropy of **1** originates from seemingly negligible SOC-induced mixing of the nonrelativistic ground state $^3A_{2g}$ with an orbitally nearly doubly degenerate excited state ^3E_g that lies ∼1800 cm^{-1} above $^3A_{2g}$. Consequently, the low-lying magnetic triplet contains 2−4% of ^3E_g, which results in a large, positive magnetic anisotropy. For the same reason, $g_{\perp}$ is substantially greater than 2, and $g_{\parallel}$ is lower than 2. This analysis is extended to related complexes to identify general characteristics of their magneto-structural correlations. Based on this analysis, we propose the criterion in Table 1 to identify the degree of ground-level orbital near-degeneracy by the symmetry of the electronic ***g***-tensor and the sign of D.

The significance of the established criteria extends far beyond the characterization of the complexes discussed here. Rather, they can be used to qualitatively characterize the electronic structures of a broad range of transition-metal complexes with low coordination number. Since both the magnetism as well as the chemical properties of metal complexes depend on their electronic structure, the criteria developed herein can make an important contribution to the characterization of novel complexes and may in combination with quantum chemical calculations guide knowledge-based synthesis approaches.

ASSOCIATED CONTENT

Supporting Information

The Supporting Information is available free of charge at https://pubs.acs.org/doi/10.1021/jacsau.4c01256.

FD-FT THz-EPR spectra; magnetometry data; details on the derivation of the effective Hamiltonian, and CASSCF(8,12)/NEVPT2 calculations on complexes **1**, **4** and **5** (PDF)

AUTHOR INFORMATION

Corresponding Authors

Liang Deng − *State Key Laboratory of Organometallic Chemistry, Shanghai Institute of Organic Chemistry, University of Chinese Academy of Sciences, Chinese Academy of Sciences, Shanghai 200032, China;* orcid.org/0000-0002-0964-9426; Email: deng@sioc.ac.cn

Alexander Schnegg − *EPR Research Group, Max Planck Institute for Chemical Energy Conversion, D-45470 Mülheim an der Ruhr, Germany; EPR4Energy Joint Lab, Department Spins in Energy Conversion and Quantum Information Science, Helmholtz-Zentrum Berlin für Materialien und Energie GmbH, 12489 Berlin, Germany;* orcid.org/0000-0002-2362-0638; Email: alexander.schnegg@cec.mpg.de

Shengfa Ye − *State Key Laboratory of Catalysis, Dalian Institute of Chemical Physics, Chinese Academy of Sciences, Dalian 116023, China; Key Laboratory of Bioinorganic and Synthetic Chemistry of Ministry of Education, Guangdong Basic Research Center of Excellence for Functional Molecular Engineering, School of Chemistry, IGCME, Sun Yat-Sen University, Guangzhou 510275, China;* orcid.org/0000-0001-9747-1412; Email: yeshf6@mail.sysu.edu.cn

Authors

Wang Chen − *State Key Laboratory of Catalysis, Dalian Institute of Chemical Physics, Chinese Academy of Sciences, Dalian 116023, China; University of Chinese Academy of Sciences, Beijing 100049, China*

Nikolai Kochetov − *EPR Research Group, Max Planck Institute for Chemical Energy Conversion, D-45470 Mülheim an der Ruhr, Germany; EPR4Energy Joint Lab, Department Spins in Energy Conversion and Quantum Information Science, Helmholtz-Zentrum Berlin für Materialien und Energie GmbH, 12489 Berlin, Germany*

Thomas Lohmiller − *EPR4Energy Joint Lab, Department Spins in Energy Conversion and Quantum Information Science, Helmholtz-Zentrum Berlin für Materialien und Energie GmbH, 12489 Berlin, Germany; Institut für Chemie, Humboldt−Universität zu Berlin, 12489 Berlin, Germany;* orcid.org/0000-0003-0373-1506

Qing Liu − *State Key Laboratory of Organometallic Chemistry, Shanghai Institute of Organic Chemistry, University of Chinese Academy of Sciences, Chinese Academy of Sciences, Shanghai 200032, China*

Complete contact information is available at: https://pubs.acs.org/10.1021/jacsau.4c01256

Author Contributions

○W.C. and N.K. contributed equally to this work. All authors have given approval to the final version of the manuscript. CRediT: **Wang Chen** data curation, formal analysis, investigation, methodology, software, validation, writing - original draft, writing - review & editing; **Nikolai Kochetov** data curation, formal analysis, investigation, methodology, visualization, writing - original draft, writing - review & editing; **Thomas Lohmiller** data curation, formal analysis, investigation, methodology, writing - original draft, writing - review & editing; **Qing Liu** investigation, methodology; **Liang Deng** funding acquisition, investigation, project administration, supervision, visualization, writing - original draft, writing - review & editing; **Alexander Schnegg** conceptualization, data curation, formal analysis, funding acquisition, investigation, methodology, supervision, validation, writing - original draft, writing - review & editing; **Shengfa Ye** conceptualization, data curation, formal analysis, funding acquisition, investigation, methodology, project administration, software, supervision, validation, visualization, writing - original draft, writing - review & editing.

Funding

Open access funded by Max Planck Society.

Notes

The authors declare no competing financial interest.

■ ACKNOWLEDGMENTS

This work is dedicated to our lovely colleague, friend and mentor, Dr. Eckhard Bill, who suddenly passed away three years ago. The work in Dalian and Guangzhou was supported by the National Natural Science Foundation of China (Nos. 22488101, 92161204 and 92461311) and by Dalian Institute of Chemical Physics, Chinese Academy of Sciences (Grant: DICP I202312). We acknowledge Helmholtz Zentrum Berlin für Materialien und Energie for the allocation of synchrotron radiation beamtime at BESSY II and thank Dirk Ponwitz and Karsten Holldack (Helmholtz-Zentrum Berlin) for their help with the FD-FT THz-EPR measurements. T.L. acknowledges support by Deutsche Forschungsgemeinschaft (DFG, German Research Foundation, Project No. LO 2898/1-1). A.S. and N.K. gratefully acknowledge funding through DFG CRC 1487 "iron upgraded" and the Max Planck Institute for Chemical Energy Conversion. L.D. thanks the financial support from the National Natural Science Foundation of China (Nos. 22231010 and 92461311), the Strategic Priority Research Program of the Chinese Academy of Sciences (XDB0610000), and the Shanghai Science and Technology Development Funds (22JC1403400).

■ REFERENCES

(1) (a) Yang, X.-F.; Wang, A.; Qiao, B.; Li, J.; Liu, J.; Zhang, T. Single-Atom Catalysts: A New Frontier in Heterogeneous Catalysis. *Acc. Chem. Res.* **2013**, *46* (8), 1740−1748. (b) Yi, Z.; Lin, L.; Chang, Y.; Luo, X.; Gao, J.; Mu, R.; Ning, Y.; Fu, Q.; Bao, X. Dynamic Transformation between Bilayer Islands and Dinuclear Clusters of Cr Oxide on Au(111) through Environment and Interface Effects. *Proc. Natl. Acad. Sci. U.S.A.* **2022**, *119* (22), No. e2120716119. (c) Xin, H.; Lin, L.; Li, R.; Li, D.; Song, T.; Mu, R.; Fu, Q.; Bao, X. Overturning CO_2 Hydrogenation Selectivity with High Activity Via Reaction-Induced Strong Metal−Support Interactions. *J. Am. Chem. Soc.* **2022**, *144* (11), 4874−4882. (d) Dong, J.; Fu, Q.; Jiang, Z.; Mei, B.; Bao, X. Carbide-Supported Au Catalysts for Water−Gas Shift Reactions: A New Territory for the Strong Metal−Support Interaction Effect. *J. Am. Chem. Soc.* **2018**, *140* (42), 13808−13816. (e) Qiao, B.; Wang, A.; Yang, X.; Allard, L. F.; Jiang, Z.; Cui, Y.; Liu, J.; Li, J.; Zhang, T. Single-Atom Catalysis of CO Oxidation Using Pt_1/FeO_x. *Nat. Chem.* **2011**, *3* (8), 634−641. (f) Lin, J.; Wang, A.; Qiao, B.; Liu, X.; Yang, X.; Wang, X.; Liang, J.; Li, J.; Liu, J.; Zhang, T. Remarkable Performance of Ir_1/FeO_x Single-Atom Catalyst in Water Gas Shift Reaction. *J. Am. Chem. Soc.* **2013**, *135* (41), 15314−15317. (g) Liu, W.; Zhang, L.; Yan, W.; Liu, X.; Yang, X.; Miao, S.; Wang, W.; Wang, A.; Zhang, T. Single-Atom Dispersed Co−N−C Catalyst: Structure Identification and Performance for Hydrogenative Coupling of Nitroarenes. *Chem. Sci.* **2016**, *7* (9), 5758−5764. (h) Liu, W.; Zhang, L.; Liu, X.; Liu, X.; Yang, X.; Miao, S.; Wang, W.; Wang, A.; Zhang, T. Discriminating Catalytically Active Fenx Species of Atomically Dispersed Fe−N−C Catalyst for Selective Oxidation of the C−H Bond. *J. Am. Chem. Soc.* **2017**, *139* (31), 10790−10798. (i) Wang, A.; Li, J.; Zhang, T. Heterogeneous Single-Atom Catalysis. *Nat. Rev. Chem.* **2018**, *2* (6), 65−81.

(2) (a) Spatzal, T.; Perez, K. A.; Einsle, O.; Howard, J. B.; Rees, D. C. Ligand Binding to the FeMo-Cofactor: Structures of Co-Bound and Reactivated Nitrogenase. *Science* **2014**, *345* (6204), 1620−1623. (b) Kang, W.; Lee, C. C.; Jasniewski, A. J.; Ribbe, M. W.; Hu, Y. Structural Evidence for a Dynamic Metallocofactor During N_2 Reduction by Mo-Nitrogenase. *Science* **2020**, *368* (6497), 1381−1385. (c) Hoffman, B. M.; Lukoyanov, D.; Dean, D. R.; Seefeldt, L. C. Nitrogenase: A Draft Mechanism. *Acc. Chem. Res.* **2013**, *46* (2), 587−595. (d) Hoffman, B. M.; Lukoyanov, D.; Yang, Z.-Y.; Dean, D. R.; Seefeldt, L. C. Mechanism of Nitrogen Fixation by Nitrogenase: The Next Stage. *Chem. Rev.* **2014**, *114* (8), 4041−4062. (e) Harris, D. F.; Lukoyanov, D. A.; Kallas, H.; Trncik, C.; Yang, Z.-Y.; Compton, P.; Kelleher, N.; Einsle, O.; Dean, D. R.; Hoffman, B. M.; Seefeldt, L. C. Mo-, V-, and Fe-Nitrogenases Use a Universal Eight-Electron Reductive-Elimination Mechanism to Achieve N_2 Reduction. *Biochemistry* **2019**, *58* (30), 3293−3301. (f) Van Stappen, C.; Decamps, L.; Cutsail, G. E., III; Bjornsson, R.; Henthorn, J. T.; Birrell, J. A.; DeBeer, S. The Spectroscopy of Nitrogenases. *Chem. Rev.* **2020**, *120* (12), 5005−5081. (g) Van Stappen, C.; Davydov, R.; Yang, Z.-Y.; Fan, R.; Guo, Y.; Bill, E.; Seefeldt, L. C.; Hoffman, B. M.; DeBeer, S. Spectroscopic Description of the E1 State of Mo Nitrogenase Based on Mo and Fe X-Ray Absorption and Mössbauer Studies. *Inorg. Chem.* **2019**, *58* (18), 12365−12376.

(3) (a) Rodriguez, M. M.; Bill, E.; Brennessel, W. W.; Holland, P. L. N_2 Reduction and Hydrogenation to Ammonia by a Molecular Iron-Potassium Complex. *Science* **2011**, *334* (6057), 780−783. (b) Figg, T. M.; Holland, P. L.; Cundari, T. R. Cooperativity between Low-Valent Iron and Potassium Promoters in Dinitrogen Fixation. *Inorg. Chem.* **2012**, *51* (14), 7546−7550. (c) MacLeod, K. C.; Holland, P. L. Recent Developments in the Homogeneous Reduction of Dinitrogen by Molybdenum and Iron. *Nat. Chem.* **2013**, *5* (7), 559−565. (d) Chiang, K. P.; Bellows, S. M.; Brennessel, W. W.; Holland, P. L. Multimetallic Cooperativity in Activation of Dinitrogen at Iron−Potassium Sites. *Chem. Sci.* **2014**, *5* (1), 267−274. (e) MacLeod, K. C.; Vinyard, D. J.; Holland, P. L. A Multi-Iron System Capable of Rapid N_2 Formation and N_2 Cleavage. *J. Am. Chem. Soc.* **2014**, *136* (29), 10226−10229. (f) Grubel, K.; Brennessel, W. W.; Mercado, B. Q.; Holland, P. L. Alkali Metal Control over N−N Cleavage in Iron Complexes. *J. Am. Chem. Soc.* **2014**, *136* (48), 16807−16816. (g) McWilliams, S. F.; Holland, P. L. Dinitrogen Binding and Cleavage by Multinuclear Iron Complexes. *Acc. Chem. Res.* **2015**, *48* (7), 2059−2065. (h) MacLeod, K. C.; Menges, F. S.; McWilliams, S. F.; Craig, S. M.; Mercado, B. Q.; Johnson, M. A.; Holland, P. L. Alkali-Controlled C−H Cleavage or N−C Bond Formation by N_2-Derived Iron Nitrides and Imides. *J. Am. Chem. Soc.* **2016**, *138* (35), 11185−11191.

(4) Zhang, Y.; Du, P.; Ji, Y.; Wang, S.; Zhu, Y.; Liu, Z.; He, Y.; Peng, Q.; Feng, Z. Catalytic Cross-Electrophile Coupling of Aryl Chlorides with Unactivated Alkyl Chlorides: The Synergy of Iron and Li. *Chem* **2023**, *9* (12), 3623−3636.

(5) Zhang, Z.-J.; Jacob, N.; Bhatia, S.; Boos, P.; Chen, X.; DeMuth, J. C.; Messinis, A. M.; Jei, B. B.; Oliveira, J. C. A.; Radović, A.; Neidig, M. L.; Wencel-Delord, J.; Ackermann, L. Iron-Catalyzed Stereoselective C−H Alkylation for Simultaneous Construction of C−N Axial and C-Central Chirality. *Nat. Commun.* **2024**, *15* (1), No. 3503.

(6) Rowsell, B. J. S.; O'Brien, H. M.; Athavan, G.; Daley-Dee, P. R.; Krieger, J.; Richards, E.; Heaton, K.; Fairlamb, I. J. S.; Bedford, R. B. The Iron-Catalysed Suzuki Coupling of Aryl Chlorides. *Nat. Catal.* **2024**, *7*, 1186−1198.

(7) (a) Costentin, C.; Drouet, S.; Robert, M.; Savéant, J.-M. A Local Proton Source Enhances CO_2 Electroreduction to CO by a Molecular Fe Catalyst. *Science* **2012**, *338* (6103), 90−94. (b) Costentin, C.; Robert, M.; Savéant, J.-M. Catalysis of the Electrochemical Reduction of Carbon Dioxide. *Chem. Soc. Rev.* **2013**, *42* (6), 2423−2436. (c) Azcarate, I.; Costentin, C.; Robert, M.; Savéant, J.-M. Through-Space Charge Interaction Substituent Effects in Molecular Catalysis Leading to the Design of the Most Efficient Catalyst of CO_2-to-Co Electrochemical Conversion. *J. Am. Chem. Soc.* **2016**, *138* (51), 16639−16644. (d) Costentin, C.; Robert, M.; Savéant, J.-M. Current Issues in Molecular Catalysis Illustrated by Iron Porphyrins as Catalysts of the CO_2-to-Co Electrochemical Conversion. *Acc. Chem. Res.* **2015**, *48* (12), 2996−3006. (e) Costentin, C.; Robert, M.; Savéant, J.-M.; Tatin, A. Efficient and Selective Molecular Catalyst for the CO_2-to-Co Electrochemical Conversion in Water. *Proc. Natl. Acad. Sci. U.S.A.* **2015**, *112* (22), 6882−6886. (f) Costentin, C.; Passard, G.; Robert, M.; Savéant, J.-M. Ultraefficient Homogeneous Catalyst for the CO_2-to-Co Electrochemical Conversion. *Proc. Natl. Acad. Sci. U.S.A.* **2014**, *111* (42), 14990−14994. (g) Costentin, C.; Passard, G.; Robert, M.; Savéant, J.-M. Pendant Acid−Base Groups in Molecular Catalysts: H-Bond Promoters or Proton Relays? Mechanisms of the Conversion of CO_2 to Co by Electrogenerated

https://doi.org/10.1021/jacsau.4c01256
JACS Au 2025, 5, 1016−1030

Iron(0)Porphyrins Bearing Prepositioned Phenol Functionalities. *J. Am. Chem. Soc.* **2014**, *136* (33), 11821−11829. (h) Costentin, C.; Passard, G.; Savéant, J.-M. Benchmarking of Homogeneous Electrocatalysts: Overpotential, Turnover Frequency, Limiting Turnover Number. *J. Am. Chem. Soc.* **2015**, *137* (16), 5461−5467.
(8) Tarrago, M.; Römelt, C.; Nehrkorn, J.; Schnegg, A.; Neese, F.; Bill, E.; Ye, S. Experimental and Theoretical Evidence for an Unusual Almost Triply Degenerate Electronic Ground State of Ferrous Tetraphenylporphyrin. *Inorg. Chem.* **2021**, *60* (7), 4966−4985.
(9) Tarrago, M.; Ye, S.; Neese, F. Electronic Structure Analysis of Electrochemical CO_2 Reduction by Iron-Porphyrins Reveals Basic Requirements for Design of Catalysts Bearing Non-Innocent Ligands. *Chem. Sci.* **2022**, *13* (34), 10029−10047.
(10) Römelt, C.; Song, J.; Tarrago, M.; Rees, J. A.; van Gastel, M.; Weyhermüller, T.; DeBeer, S.; Bill, E.; Neese, F.; Ye, S. Electronic Structure of a Formal Iron(0) Porphyrin Complex Relevant to CO_2 Reduction. *Inorg. Chem.* **2017**, *56* (8), 4745−4750.
(11) (a) Christou, G.; Gatteschi, D.; Hendrickson, D. N.; Sessoli, R. Single-Molecule Magnets. *MRS Bull.* **2000**, *25* (11), 66−71. (b) Murrie, M. Cobalt(II) Single-Molecule Magnets. *Chem. Soc. Rev.* **2010**, *39* (6), 1986−1995. (c) Layfield, R. A. Organometallic Single-Molecule Magnets. *Organometallics* **2014**, *33* (5), 1084−1099. (d) Holynska, M. *Single-Molecule Magnets: Molecular Architectures and Building Blocks for Spintronics*; John Wiley & Sons, 2019. (e) Atanasov, M.; Aravena, D.; Suturina, E.; Bill, E.; Maganas, D.; Neese, F. First Principles Approach to the Electronic Structure, Magnetic Anisotropy and Spin Relaxation in Mononuclear 3d-Transition Metal Single Molecule Magnets. *Coord. Chem. Rev.* **2015**, *289*−*290*, 177−214. (f) Craig, G. A.; Murrie, M. 3d Single-Ion Magnets. *Chem. Soc. Rev.* **2015**, *44* (8), 2135−2147. (g) Frost, J. M.; Harriman, K. L. M.; Murugesu, M. The Rise of 3d Single-Ion Magnets in Molecular Magnetism: Towards Materials from Molecules? *Chem. Sci.* **2016**, *7* (4), 2470−2491.
(12) (a) Zadrozny, J. M.; Xiao, D. J.; Long, J. R.; Atanasov, M.; Neese, F.; Grandjean, F.; Long, G. J. Mössbauer Spectroscopy as a Probe of Magnetization Dynamics in the Linear Iron(I) and Iron(II) Complexes $[Fe(C(SiMe_3)_3)_2]^{1-/0}$. *Inorg. Chem.* **2013**, *52* (22), 13123−13131. (b) Atanasov, M.; Zadrozny, J. M.; Long, J. R.; Neese, F. A Theoretical Analysis of Chemical Bonding, Vibronic Coupling, and Magnetic Anisotropy in Linear Iron(II) Complexes with Single-Molecule Magnet Behavior. *Chem. Sci.* **2013**, *4* (1), 139−156. (c) Weller, R.; Atanasov, M.; Demeshko, S.; Chen, T.-Y.; Mohelsky, I.; Bill, E.; Orlita, M.; Meyer, F.; Neese, F.; Werncke, C. G. On the Single-Molecule Magnetic Behavior of Linear Iron(I) Arylsilylamides. *Inorg. Chem.* **2023**, *62* (7), 3153−3161. (d) Zadrozny, J. M.; Xiao, D. J.; Atanasov, M.; Long, G. J.; Grandjean, F.; Neese, F.; Long, J. R. Magnetic Blocking in a Linear Iron(I) Complex. *Nat. Chem.* **2013**, *5* (7), 577−581.
(13) (a) Bunting, P. C.; Atanasov, M.; Damgaard-Møller, E.; Perfetti, M.; Crassee, I.; Orlita, M.; Overgaard, J.; van Slageren, J.; Neese, F.; Long, J. R. A Linear Cobalt(II) Complex with Maximal Orbital Angular Momentum from a Non-Aufbau Ground State. *Science* **2018**, *362* (6421), No. eaat7319. (b) Meng, Y.-S.; Mo, Z.; Wang, B.-W.; Zhang, Y.-Q.; Deng, L.; Gao, S. Observation of the Single-Ion Magnet Behavior of d^8 Ions on Two-Coordinate Co(I)−NHC Complexes. *Chem. Sci.* **2015**, *6* (12), 7156−7162. (c) Yao, X.-N.; Du, J.-Z.; Zhang, Y.-Q.; Leng, X.-B.; Yang, M.-W.; Jiang, S.-D.; Wang, Z.-X.; Ouyang, Z.-W.; Deng, L.; Wang, B.-W.; Gao, S. Two-Coordinate Co(II) Imido Complexes as Outstanding Single-Molecule Magnets. *J. Am. Chem. Soc.* **2017**, *139* (1), 373−380.
(14) (a) Dunsford, J. J.; Evans, D. J.; Pugh, T.; Shah, S. N.; Chilton, N. F.; Ingleson, M. J. Three-Coordinate Iron(II) Expanded Ring N-Heterocyclic Carbene Complexes. *Organometallics* **2016**, *35* (8), 1098−1106. (b) Fillman, K. L.; Przyojski, J. A.; Al-Afyouni, M. H.; Tonzetich, Z. J.; Neidig, M. L. A Combined Magnetic Circular Dichroism and Density Functional Theory Approach for the Elucidation of Electronic Structure and Bonding in Three- and Four-Coordinate Iron(II)−N-Heterocyclic Carbene Complexes. *Chem. Sci.* **2015**, *6* (2), 1178−1188.
(15) (a) Jahn, H. A.; Teller, E. Stability of Polyatomic Molecules in Degenerate Electronic States-I—Orbital Degeneracy. *Proc. R. Soc. A* **1937**, *161* (905), 220−235. (b) Ham, F. S. Dynamical Jahn-Teller Effect in Paramagnetic Resonance Spectra: Orbital Reduction Factors and Partial Quenching of Spin-Orbit Interaction. *Phys. Rev.* **1965**, *138* (6A), No. A1727. (c) Kaplan, M. D.; Zimmerman, G. O. *Vibronic Interactions: Jahn-Teller Effect in Crystals and Molecules*; Springer Science & Business Media, 2001; Vol. *39*. (d) Atanasov, M.; Daul, C.; Tregenna-Piggott, P. L. *Vibronic Interactions and the Jahn-Teller Effect: Theory and Applications*; Springer Science & Business Media, 2011; Vol. *23*. (e) Bersuker, I. *The Jahn-Teller Effect and Vibronic Interactions in Modern Chemistry*; Springer Science & Business Media, 2013. (f) Köppel, H.; Yarkony, D. R.; Barentzen, H. *The Jahn-Teller Effect: Fundamentals and Implications for Physics and Chemistry*; Springer Science & Business Media, 2009; Vol. *97*.
(16) McGarvey, B. R.; Telser, J. Simple Ligand-Field Theory of d^4 and d^6 Transition Metal Complexes with a C_3 Symmetry Axis. *Inorg. Chem.* **2012**, *51* (11), 6000−6010.
(17) (a) Pilbrow, J. *Transition Ion Electron Paramagnetic Resonance*; Clarendon: Oxford, 1990. (b) Mabbs, F. E.; Collison, D. *Electron Paramagnetic Resonance of D Transition Metal Compounds*; Elsevier, 2013. (c) Abragam, A.; Bleaney, B. *Electron Paramagnetic Resonance of Transition Ions*; OUP: Oxford, 2012. (d) Weil, J. A.; Bolton, J. R. *Electron Paramagnetic Resonance: Elementary Theory and Practical Applications*; John Wiley & Sons, 2007. (e) Al'tshuler, S. A.; Kozyrev, B. M. *Electron Paramagnetic Resonance*; Academic Press, 2013. (f) Wertz, J. *Electron Spin Resonance: Elementary Theory and Practical Applications*; Springer Science & Business Media, 2012. (g) Assenheim, H. M. *Introduction to Electron Spin Resonance*; Springer, 2014. (h) Harriman, J. E. *Theoretical Foundations of Electron Spin Resonance: Physical Chemistry: A Series of Monographs*; Academic Press, 2013.
(18) (a) Zhang, H.; Ouyang, Z.; Liu, Y.; Zhang, Q.; Wang, L.; Deng, L. (Aminocarbene)(Divinyltetramethyldisiloxane)Iron(0) Compounds: A Class of Low-Coordinate Iron(0) Reagents. *Angew. Chem., Int. Ed.* **2014**, *53* (32), 8432−8436. (b) Cheng, J.; Chen, Q.; Leng, X.; Ye, S.; Deng, L. Three-Coordinate Iron(0) Complexes with N-Heterocyclic Carbene and Vinyltrimethylsilane Ligation: Synthesis, Characterization, and Ligand Substitution Reactions. *Inorg. Chem.* **2019**, *58* (19), 13129−13141.
(19) Holldack, K.; Schnegg, A. Thz Electron Paramagnetic Resonance/THz Spectroscopy at Bessy Ii. *J. Large-Scale Res. Facil. JLSRF* **2016**, *2*, No. A51.
(20) (a) Schnegg, A.; Behrends, J.; Lips, K.; Bittl, R.; Holldack, K. Frequency Domain Fourier Transform THz-EPR on Single Molecule Magnets Using Coherent Synchrotron Radiation. *Phys. Chem. Chem. Phys.* **2009**, *11* (31), 6820−6825. (b) Nehrkorn, J.; Holldack, K.; Bittl, R.; Schnegg, A. Recent Progress in Synchrotron-Based Frequency-Domain Fourier-Transform THz-EPR. *J. Magn. Reson.* **2017**, *280*, 10−19.
(21) Neese, F.; Wennmohs, F.; Becker, U.; Riplinger, C. The Orca Quantum Chemistry Program Package. *J. Chem. Phys.* **2020**, *152* (22), No. 224108.
(22) Staroverov, V. N.; Scuseria, G. E.; Tao, J.; Perdew, J. P. Comparative Assessment of a New Nonempirical Density Functional: Molecules and Hydrogen-Bonded Complexes. *J. Chem. Phys.* **2003**, *119* (23), 12129−12137.
(23) Weigend, F.; Ahlrichs, R. Balanced Basis Sets of Split Valence, Triple Zeta Valence and Quadruple Zeta Valence Quality for H to Rn: Design and Assessment of Accuracy. *Phys. Chem. Chem. Phys.* **2005**, *7* (18), 3297−3305.
(24) Grimme, S.; Ehrlich, S.; Goerigk, L. Effect of the Damping Function in Dispersion Corrected Density Functional Theory. *J. Comput. Chem.* **2011**, *32* (7), 1456−1465.
(25) Malmqvist, P.-Å.; Roos, B. O. The CASSCF State Interaction Method. *Chem. Phys. Lett.* **1989**, *155* (2), 189−194.
(26) Radoń, M.; Pierloot, K. Binding of CO, NO, and O_2 to Heme by Density Functional and Multireference Ab Initio Calculations. *J. Phys. Chem. A* **2008**, *112* (46), 11824−11832.

https://doi.org/10.1021/jacsau.4c01256
JACS Au 2025, 5, 1016−1030

(27) Angeli, C.; Cimiraglia, R.; Malrieu, J.-P. N-Electron Valence State Perturbation Theory: A Spinless Formulation and an Efficient Implementation of the Strongly Contracted and of the Partially Contracted Variants. *J. Chem. Phys.* **2002**, *117* (20), 9138−9153.
(28) Weigend, F. Hartree−Fock Exchange Fitting Basis Sets for H to Rn. *J. Comput. Chem.* **2008**, *29* (2), 167−175.
(29) Kollmar, C.; Sivalingam, K.; Helmich-Paris, B.; Angeli, C.; Neese, F. A Perturbation-Based Super-CI Approach for the Orbital Optimization of a CASSCF Wave Function. *J. Comput. Chem.* **2019**, *40* (14), 1463−1470.
(30) (a) Nehrkorn, J.; Telser, J.; Holldack, K.; Stoll, S.; Schnegg, A. Simulating Frequency-Domain Electron Paramagnetic Resonance: Bridging the Gap between Experiment and Magnetic Parameters for High-Spin Transition-Metal Ion Complexes. *J. Phys. Chem. B* **2015**, *119* (43), 13816−13824. (b) Stoll, S.; Schweiger, A. Easyspin, a Comprehensive Software Package for Spectral Simulation and Analysis in EPR. *J. Magn. Reson.* **2006**, *178* (1), 42−55.
(31) Bone, A. N.; Widener, C. N.; Moseley, D. H.; Liu, Z.; Lu, Z.; Cheng, Y.; Daemen, L. L.; Ozerov, M.; Telser, J.; Thirunavukkuarasu, K.; Smirnov, D.; Greer, S. M.; Hill, S.; Krzystek, J.; Holldack, K.; Aliabadi, A.; Schnegg, A.; Dunbar, K. R.; Xue, Z.-L. Applying Unconventional Spectroscopies to the Single-Molecule Magnets, $Co(PPh_3)_2X_2$ (X = Cl, Br, I): Unveiling Magnetic Transitions and Spin-Phonon Coupling. *Chem. - Eur. J.* **2021**, *27* (43), 11110−11125.
(32) Lohmiller, T.; Spyra, C.-J.; Dechert, S.; Demeshko, S.; Bill, E.; Schnegg, A.; Meyer, F. Antisymmetric Spin Exchange in a μ-1,2-Peroxodicopper(II) Complex with an Orthogonal Cu−O−O−Cu Arrangement and S = 1 Spin Ground State Characterized by THz-EPR. *JACS Au* **2022**, *2* (5), 1134−1143.
(33) Wolford, N. J.; Muñoz Iii, S. B.; Neate, P. G. N.; Brennessel, W. W.; Neidig, M. L. NHC Effects on Reduction Dynamics in Iron-Catalyzed Organic Transformations. *Chem. - Eur. J.* **2021**, *27* (54), 13651−13658.
(34) Chibotaru, L. F.; Ungur, L. Ab Initio Calculation of Anisotropic Magnetic Properties of Complexes. I. Unique Definition of Pseudospin Hamiltonians and Their Derivation. *J. Chem. Phys.* **2012**, *137* (6), No. 064112.
(35) Griffith, J. S. *The Theory of Transition-Metal Ions*; Cambridge University Press, 1961.
(36) (a) Lin, W. C. d-orbital Energies and Low-Lying Excited States of Cobalt Porphyrins. *Inorg. Chem.* **1976**, *15* (5), 1114−1118. (b) Boyd, P. D. W.; Buckingham, D. A.; McMeeking, R. F.; Mitra, S. Paramagnetic Anisotropy, Average Magnetic Susceptibility, and Electronic Structure of Intermediate-Spin S = 1 (5,10,15,20-Tetraphenylporphyrin)Iron(II). *Inorg. Chem.* **1979**, *18* (12), 3585−3591.
(37) Neese, F.; Solomon, E. I. Calculation of Zero-Field Splittings, g-Values, and the Relativistic Nephelauxetic Effect in Transition Metal Complexes. Application to High-Spin Ferric Complexes. *Inorg. Chem.* **1998**, *37* (26), 6568−6582.
(38) Xiong, J.; Liu, Q.; Lavina, B.; Hu, M. Y.; Zhao, J.; Alp, E. E.; Deng, L.; Ye, S.; Guo, Y. Spin Polarization Assisted Facile C−H Activation by an S = 1 Iron(IV)−Bisimido Complex: A Comprehensive Spectroscopic and Theoretical Investigation. *Chem. Sci.* **2023**, *14* (11), 2808−2820.
(39) Andres, H.; Bominaar, E. L.; Smith, J. M.; Eckert, N. A.; Holland, P. L.; Münck, E. Planar Three-Coordinate High-Spin Fe^{II} Complexes with Large Orbital Angular Momentum: Mössbauer, Electron Paramagnetic Resonance, and Electronic Structure Studies. *J. Am. Chem. Soc.* **2002**, *124* (12), 3012−3025.
(40) Nagelski, A. L.; Ozerov, M.; Fataftah, M. S.; Krzystek, J.; Greer, S. M.; Holland, P. L.; Telser, J. Electronic Structure of Three-Coordinate Fe^{II} and Co^{II} β-diketiminate Complexes. *Inorg. Chem.* **2024**, *63* (10), 4511−4526.
(41) Chang, H.-C.; Mondal, B.; Fang, H.; Neese, F.; Bill, E.; Ye, S. Electron Paramagnetic Resonance Signature of Tetragonal Low Spin Iron(V)-Nitrido and -Oxo Complexes Derived from the Electronic Structure Analysis of Heme and Non-Heme Archetypes. *J. Am. Chem. Soc.* **2019**, *141* (6), 2421−2434.
(42) (a) Wang, D.; Chen, W.; Zhai, C.; Zhao, L.; Ye, S.; Tan, G. Monosubstituted Doublet Sn(I) Radical Featuring Substantial Unquenched Orbital Angular Momentum. *J. Am. Chem. Soc.* **2023**, *145* (12), 6914−6920. (b) Chen, H.; Chen, W.; Wang, D.; Chen, Y.; Liu, Z.; Ye, S.; Tan, G.; Gao, S. An Isolable One-Coordinate Lead(I) Radical with Strong g-Factor Anisotropy. *Angew. Chem., Int. Ed.* **2024**, *63* (20), No. e202402093.
(43) (a) Walker, F. A. Electron Spin Resonance Study of Coordination to the Fifth and Sixth Positions Of.Alpha.,.Beta.,.Gamma.,.Delta.-Tetra(P-Methoxyphenyl)Porphinatocobalt(II). *J. Am. Chem. Soc.* **1970**, *92* (14), 4235−4244. (b) Ann Walker, F. ESR Studies of Co(II) Tetraphenylporphyrins and Their Oxygen Adducts: Complex Formation with Aromatic Molecules and Sterically Hindered Lewis Bases. *J. Magn. Reson.* **1974**, *15* (2), 201−218. (c) Walker, F. A. Steric and Electronic Effeccts in the Coordination of Amines to a Cobalt (II) Porphyrin. *J. Am. Chem. Soc.* **1973**, *95* (4), 1150−1153. (d) La Mar, G. N.; Walker, F. A. Proton Nuclear Magnetic Resonance and Electron Spin Resonance Investigation of Axial Solvation in Planar, Low-Spin Cobalt (II) Porphyrin Complexes. *J. Am. Chem. Soc.* **1973**, *95* (6), 1790−1796.
(44) (a) Wayland, B. B.; Sherry, A. E.; Bunn, A. G. EPR Studies of 1:1 Complexes of Rhodium(II) and Cobalt(II) Porphyrins With.-Sigma. Donor And.Pi. Acceptor Ligands: Origins of Rhodium(II) Metalloradical Reactivity. *J. Am. Chem. Soc.* **1993**, *115* (17), 7675−7684. (b) Zhang, X.-X.; Wayland, B. B. Sterically Demanding Diporphyrin Ligands and Rhodium(II) Porphyrin Bimetalloradical Complexes. *Inorg. Chem.* **2000**, *39* (23), 5318−5325. (c) De Bruin, B.; Hetterscheid, D. G.; Koekkoek, A. J.; Gruetzmacher, H. The Organometallic Chemistry of Rh-, Ir-, Pd-, and Pt-Based Radicals: Higher Valent Species. *Prog. Inorg. Chem.* **2007**, *55*, 247−354. (d) Sherry, A. E.; Wayland, B. B. Metalloradical Activation of Carbon Monoxide. Formation and Carbonyl Coupling of a Bent 17 Electron M-CO Unit. *J. Am. Chem. Soc.* **1989**, *111* (13), 5010−5012. (e) Collman, J. P.; Boulatov, R. Synthesis and Reactivity of Porphyrinatorhodium(II)−Triethylphosphine Adducts: The Role of PEt_3 in Stabilizing a Formal Rh(II) State. *J. Am. Chem. Soc.* **2000**, *122* (48), 11812−11821.

https://doi.org/10.1021/jacsau.4c01256
JACS Au 2025, 5, 1016−1030